T.C.

MARMARA UNIVERSITY

INSTITUTE FOR GRADUATE STUDIES IN

PURE AND APPLIED SCIENCES

THE DIRECTIONAL SOLIDIFICATION AND MICROSEGREGATION IN LOW ALLOY STEELS

Özgür Çēnar

(Materials&Metallurgy Engineering)

THESIS

FOR THE DEGREE OF MASTER OF SCIENCE

IN

MATERIALS SCIENCE AND ENGINEERING PROGRAMME

SUPERVISOR
Doç.Dr. Altan Türkeli

ISTANBUL 2007

T.C.

MARMARA UNIVERSITY

INSTITUTE FOR GRADUATE STUDIES IN

PURE AND APPLIED SCIENCES

THE DIRECTIONAL SOLIDIFICATION AND MICROSEGREGATION IN LOW ALLOY STEELS

Özgür ÇINAR

(Materials&Metallurgy Engineering)

141103520030126

THESIS

FOR THE DEGREE OF MASTER OF SCIENCE

IN

MATERIALS SCIENCE AND ENGINEERING PROGRAMME

SUPERVISOR
Doç.Dr. Altan TÜRKELĶ

ISTANBUL 2007

MARA UNIVERSITY

E INSTITUTE FOR

GRADUATE STUDIES IN PURE AND APPLIED SCIENCES

ACCEPTANCE AND APPROVAL DOCUMENT

THE DIRECTIONAL SOLIDIFICATION AND MICROSEGREGATION IN LOW ALLOY

Established committee listed below, on 17/07/2007 and 2007/11-13 by the *INSTITUTE FOR GRADUATE STUDIES IN PURE AND APPLIED SCIENCES*ô Executive Committee, have accepted Mr. Özgür Çēnarós Master of Science / Doctor of Philosophy thesis, titled as ñThe Directional Solidification and Microsegregation In Low Alloy Steel in Metallurgical and Material Engineering.

COMMITTEE

Advisor : Prof. Dr. Altan Türkeli é é é é é é é é

Member : Yrd. Doç. Dr. Kenan Yēldēzé é é é é é é é

Member : Yrd. Doç. Dr. Seval Gençé é é é é é é é é .

Date of thesisô/ dissertationôs defense before the committee:17/07/2007

APPROVAL

Mr. Özgür Çēnar has satisfactorily completed the requirements for the degree of Doctor of Philosophy / Master of Science in ..... at Marmara University.
Mr. / Mrs. / Miss. ..... is eligible to have the degree awarded at our convocation on ..... Diploma and transcripts so noted will be available after that date.

Istanbul **DIRECTOR**

To my wife ,Zuhal ÇINAR

ACKNOWLEDGEMENTS

I wish to thank my advisor, Assoc. Dr. Atlan Türkeli, for his patience, guidance, and encouragement throughout this thesis. I would like to thank to the Chairman of Material Science and Engineering Department, Prof. Dr. Arif N. Güllüoğlu and the Dean of Engineering Faculty of Marmara University, Prof. Dr. Ahmet Alp Sayar for their permission to use the facilities of enginerring faculty.

My special thanks go to Dr. Müh. Yzb. Alpay Yılmaz and Yük. Müh. Üst. Halil M. Coşkun for helping me both within and out of the experimental processes. I wish to express my thanks to Hamdi Yel and the employees of 1013 Maintenance Unit.

I am thankful to Işıl Küçük and Mehmet Ali Yorulmaz for all her help, support, assistance and friendship. I would like to thank my committee members; Ass. Dr. Seval Genç, Ass. D. Kenan Yıldız, Ass. Dr. Recep Artır, for their interest and discussions. I wish to express my thanks to Yük. Müh. Mustafa Işıkhan with his help during the SEM usage.

June, 2007 **Özgür ÇINAR**

CONTENTS

ÖZET

DÜŞÜK ALAŞIMLI ÇELİKLERDE YÖNLENDİRİLMİŞ KATILAŞMA VE MİKROSEGREGASYON

Dünyada her yıl yedi yüz milyon tondan fazla çelik üretilmektedir. Bu çeliklerin büyük çoğunluğu karbon ve düşük alaşımlı çeliklerden oluşmaktadır. Üretim boyunca oluşan mikro yapısı ve inklizyon oluşumu çeliklerin mekanik özelliklerini etkilemektedir. Bu yüzden çeliklerin katılaşma mekanizmalarını anlamak önem arz etmektedir.

Dengesiz katılaşma sonucunda dendritik ve hücresel mikro yapılarında mikrosegregasyon oluşur ve bu mikrosegregasyonda; döküm yapılarının korozyon, mekanik özellikleri, faz dönüşümleri, bantlaşma yapıları, ötektik faz miktarı, çözeltiye alma ve homojenleştirme ısıl işlemleri gibi fiziksel ve kimyasal özellikleri etkilidir.

Bu çalışmada %0,4 C, %0,7 Mn, %0,25 Si, %1Cr, %0,25 Mo içeren 4140 düşük alaşım çeliği, kolonsal dendritik yapı elde etmek için yönlendirerek katılaştırılmıştır. Kolonsal yetmiş tane dendritik yapısı optik ve elektron mikroskobuyla incelenmiştir. İkincil dendritik kollar arası mesafenin çil bölgesinde 30 mikron kolonsal 70 tane son bölgesine kadar 85 mikron olarak arttığı tespit edilmiştir.Temel alaşım elementleri olan Cr, Mn, Moʼnin mikrosegregasyonu çizgi analiziyle analiz edilmiştir. Birincil kollar arasındaki çözelti elementlerinin dağılımı, ikincil dendritik kolların arasındaki çözelti elementlerin dağılımından çok az daha yüksek olduğu bulunmuştur.

Temmuz, 2007 **Özgür ÇINAR**

ABSTRACT

THE DIRECTIONAL SOLIDIFICATION AND MICROSEGREGATION IN LOW ALLOY STEELS.

Steel is produced more than 700 million tons all around the world every year. Most of these products are carbon or low-alloy steels. Microstructures and formation of inclusions during production affect the mechanical properties of steels. Therefore, the understanding of the solidification mechanism of steels is important.

Microsegregation occurs in dendritic and cellular microstructures as a result of non-equilibrium solidification and can affect physical and chemical properties of cast structures, such as corrosion, mechanical properties, phase transformations, banding structure, amount of eutectic phase, solution and homogenization heat treatments.

In this study, 4140 low alloy steel, which contains 0.40 wt % C, 0.70 wt % Mn, 0.25 wt % Si, 1 wt % Cr, and 0.2 wt % Mo, is directionally solidified to obtain columnar dendrites. Its dendritic structure of columnar zone is investigated with optical microscope and scanning electron microscope (SEM). It is found that secondary dendrite arm spacing increases from 30 micron at the chill to 85 micron at the end of columnar zone. We also analyzed microsegregation of major solute elements (Cr, Mn, and Mo) with line-analysis. It is found that segregation of solute elements between primary arms is slightly higher than between secondary arms.

July,2007 **Özgür ÇINAR**

LIST OF SYMBOLS

$æG_{(r)}$	: Free Energy Change For A Single Nucleus
$æG^*$	: Critical Free Energy To Nucleation
$æG_{het}^*$	: Critical Free Energy To Heterogeneous Nucleation
$æG_{hom}^*$	: Critical Free Energy To Homogeneous Nucleation
$æG_v$	: Volume Free Energy
$æH_v$	: Change In Enthalpy Of Solidification
æT	: Undercooling
æTk	: Molecular Attachment Kinetics Is The Interface Supercooling
B	: Back Diffusion Coefficient In The Solid Phase
C^0_m	: Minimum Solute Content
C^0_M	: Maximum Solute Content
C_E	: Eutectic Composition
C_L	: Compositions In The Liquid
CMax	: Maximum Composition
Co	: Initial Alloy Composition
C_S	: Solute Compositions In The Solid
C_{SM}	: Solubility In The Solid Solution
D_L	: Diffuse In The Liquid
f_S	: Volume Fraction Of Solid
g_L	: Volume Fractions Of Liquid
g_s	: Volume Fractions Of Solid
k	: Partition Coefficient
k_{ef}	: Effective Distribution Coefficient

t_f : Final Solidification Time

t_f : Local Solidification Time

T_m : Melting Temperature

V : Velocity

V_0 : Initial Velocity

$\check{U}$: Dimensionless Back-Diffusion Coefficient

σ_{SL} : Solid/Liquid Interfacial Energy

$\check{u}_s$: Mass Balance For The Boundary Layer

λ : Dendrite Arm Spacing

λ_1 : Primary Arm Spacing

λ_2 : Secondary Arm Spacing

λ_f : Final Arm Spacing

λ_0 : Initial Spacing

DAS : Dendrite Arm Spacing

MP :Microprobe

SEM :Scanning Electron Microscope

S-L : Solid-Liquid

LIST OF FIGURES

PAGE

PAGE

PAGE

PAGE

LIST OF TABLES

PAGE

INTRODUCTION AND OBJECTIVES

I.1.INTRODUCTION

Plain-carbon steels are very satisfactory where strength and other requirements are not too severe. They are also used successfully at ordinary temperatures and in atmospheres that are not highly corrosive, but their relatively low hardenability limits the strength that can be obtained except in fairly thin sections. Almost all hardened steels are tempered to reduce internal stresses. It is well known that plain-carbon steels show a marked softening with increasing tempering temperature. This behavior will lessen their applicability for parts that require hardness above room temperature. Most of the limitations of plain-carbon steels may be overcome by the use of alloying elements.

An *alloy steel* may be defined as one whose characteristic properties are due to some element other than carbon. Although all plain-carbon steels contain moderate amounts of manganese (up to about 0.90 percent) and silicon (up to about 0.30 percent), they are not considered alloy steels because the principal function of the manganese and silicon is to act as deoxidizers. They combine with oxygen and sulfur to reduce the harmful effect of those elements.

Alloying elements are added to steels for many purposes. Some of the most important are:

1 Increase hardenability
2 Improve strength at ordinary temperatures
3 Improve mechanical properties at both high and low temperatures
4 Improve toughness at any minimum hardness or strength

7 Improve magnetic properties

In this study, microrosegregation and distribution of some major alloying elements, such Mn, Cr, and Mo are investigated in directionally solidified 4140 low alloy steel.

GENERAL BACKGROUND

II.1.NUCLEATION

Nucleation during solidification can be defined as the formation of a small crystal from the melt that is capable of continued growth. From a thermodynamic point of view the establishment of S-L interface is not very easy. Although the solid phase has a lower free energy than the liquid phase below Tm a small solid particle is not necessarily stable because of the free energy associated with the S-L interface. The change in free energy corresponding to the liquid-solid transition must therefore include not only the change in free energy between the two phases but also the free energy of the S-L interface. From a kinetic point of view it is possible to arrive at the same result on the basis that the atoms at the surface of a very small crystal have a higher energy than the surface atoms of a larger crystal. Therefore, the equilibrium temperature at which atoms arrive and leave at the same rate is lower for a very small crystal than for a larger one. [1]

Consequently for each temperature below Tm a solid particle can be in equilibrium with the liquid when its radius of curvature has a particular value, known as the critical radius. Because at higher supercooling there is more bulk free energy to compensate for the surface free energy, the critical radius decreases with increasing supercooling. On the other hand, at any supercooling, there exists within the melt a statistical distribution of atom clusters or embryos of different sizes having the character of the solid phase. The probability of finding an embryo of a given size increases as the temperature decreases. Nucleation occurs when the supercooling is such that there are sufficient embryos with a radius larger than the critical radius so we can see different types of nucleation that are heterogeneous and homogeneous. [1]

ation

This section deals with the simplest nucleation event, namely the homogeneous nucleation of solid crystals during the freezing of a pure metal. On completion, we should be able to:

- explain the term *homogeneous,* as applied to nucleation events,
- understand the concept of a critical size or radius, *r** and a critical free energy to nucleation, æ*G**,
- differentiate between unstable clusters (or embryos) and stable nuclei,
- derive expressions for *r** and æ*G** in terms of both volume free energy, æG_v and undercooling, æ*T*.

The section starts by explaining that a driving force for solidification, æG_v exists below the equilibrium melting temperature, T_m and that this is approximately proportional to the degree of undercooling æ*T* as seen in **Equation II.1**.;

$$\Delta G_V = \frac{\Delta H_V \Delta T}{T_m} \qquad \text{(II.1)}$$

Where æH_v is the change in enthalpy of solidification. Throughout this equation, the convention that æG_v and æH_v are NEGATIVE below T_m is used.)

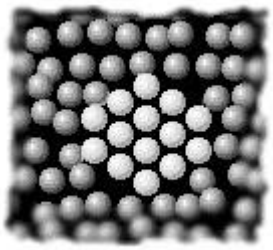

Figure II.1 The concept of small clusters of crystallized solid forming from a liquid metal. [1]

Figure II.1 is illustrated on an atomic scale the concept of small clusters of crystallized solid forming from a liquid metal. These arise due to the random motion of atoms within the liquid. By assuming that solid phase nucleates as spherical óclustersô of radius, *r*, it is shown that the net (excess) free energy change for a single nucleus, æ$G_{(r)}$ is given by **Equation II.2**;

$$\Delta G_{(\gamma)} = \frac{4}{3}\pi r^3 \Delta G_V + 4\pi r^2 \gamma_{SL} \qquad \text{(II. 2)}$$

Where ↄSL is the solid/liquid interfacial energy. The **figure II.2** shows the radius energy differentiation.

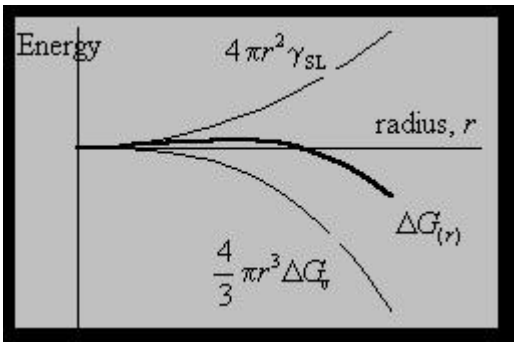

Figure II.2 Free energy change with respect to radius

The critical radius *r** (defined as the radius at which æ$G_{(r)}$ is maximum) is given by **Equation II.3**

$$r^* = \frac{-2\gamma_{SL}}{\Delta G_V} = \frac{-2\gamma_{SL} T_m}{\Delta H_V \Delta T} \qquad \text{(II.3)}$$

The associated energy barrier to homogeneous nucleation, æ*G** is found by substituting *r** into **Equation (II.4):** [1]

$$\Delta G^* = \frac{16\pi\gamma_{SL}^3}{3\Delta G_V^2} = \frac{16\pi\gamma_{SL}^3 T_m^2}{\Delta H_V^2 \Delta T^2} \qquad \text{(II.4)}$$

ation

This section continues to look at the liquid-solid transformation, but now introduces the idea that nuclei can form at preferential sites (e.g. mould wall, impurities or catalysts, etc.). The energy barrier to nucleation, æ*G** can be substantially reduced. On completion we should be able to:

- list some typical heterogeneous nucleation sites for solidification,[2]
- identify all the relevant interfacial energy terms for a heterogeneous nucleus forming as a spherical cap on a planar surface,
- Understand the term wetting, or contact angle, ɗ with respect to this geometry.
- prove that the critical nucleus size, *r** is the same for both heterogeneous and homogeneous nucleation,
- derive an equation for the æ*G** which takes into accounts nucleus geometry via the shape factor, *S*(ɗ), and in so doing show that the energy barrier to nucleation, the the æ*G** is lower for heterogeneous nucleation than for homogeneous nucleation for all contact angles less than 180°,
- explain why the wetting angle is a measure of the ócfficiencyô of a particular nucleation site,
- Write an expression relating the critical volumes of heterogeneous and homogeneous nuclei.

The main example considers a solid cluster forming on a mould wall. An exercise is provided to identify on a diagram the newly created interfaces (i.e. solid-liquid and solid-mould) and the destroyed interface (liquid-mould). These extra interfacial energy terms are incorporated into **Equation II.5**, such that: [1]

$$\Delta G_{(\gamma)} = V\Delta G_V + A_{SL}\gamma_{SL} + A_{SM}\gamma_{SM} - A_{SM}\gamma_{ML} \qquad \text{(II.5)}$$

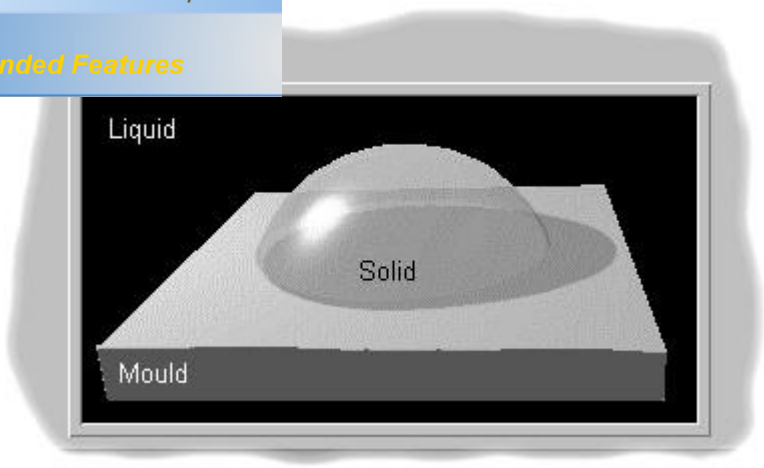

Figure II.3 Liquid wetting on the solid surface [1]

According to **Figure II.3** the manipulation of replacing can be done the volume and area terms for a spherical cap, radius r and wetting angle, until arriving at the final expressions is seed in **Equations II.6,7 and 8**; [1]

$$r_{het}^{*} = \frac{-2\gamma_{SL}}{\Delta G_V} = r_{\text{hom}}^{*} \qquad \text{(II.6)}$$

And

$$\Delta G_{\text{het}}^{*} = \frac{16\pi\gamma_{\text{SL}}^{3}}{3\Delta G_{\text{v}}^{2}} S(\theta) = \Delta G_{\text{hom}}^{*} S(\theta) \qquad \text{(II.7)}$$

Where the shape factor *S*(d) is given by:

$$S(\theta) = \frac{(2+\cos\theta)(1-\cos\theta)^2}{4} \qquad \text{(II.8)}$$

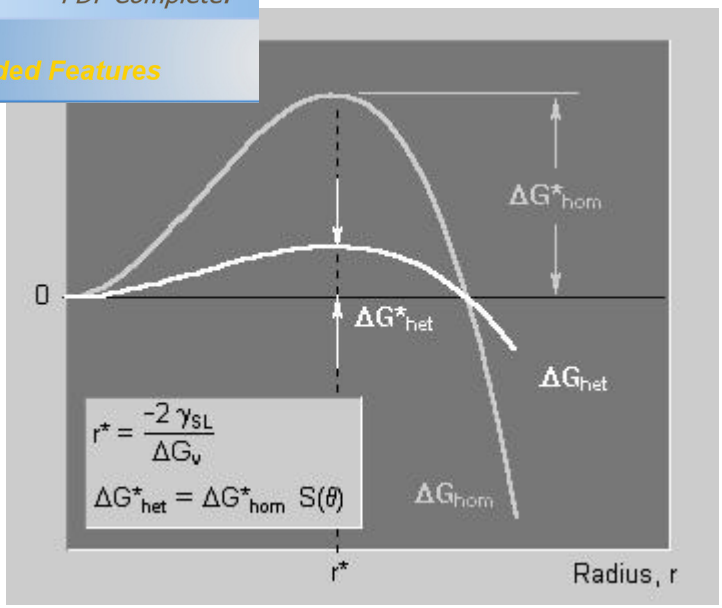

Figure II.4 Change in Gibbs free energy with respect to radius. [1]

It is defined in **Figure II.4**, the critical radius *r** is the same for both homogeneous and heterogeneous nucleation. However, due to the shape factor, the volume of a critical nucleus can be significantly smaller for heterogeneous nucleation, depending on the wetting angle ɗ. [1]

II. 2. SOLID-LIQUID INTERFACE MORPHOLOGY

The nature of the S-L interface and the rate at which atoms attempt to join the crystal can have a decisive influence on the kinetics and morphology of crystal growth. For solidification of a pure material, the parameter which governs the atomic or molecular attachment kinetics is the interface supercooling, *ΔTk*, which is the difference between the thermodynamic melting point and the interface temperature.

An interface can advance by two basic processes depending on the nature of the S-L interface;

(i) Non-uniform growth (or lateral growth) advances the interface by lateral motion of steps that are typically interplanar distances in height. An atom or molecule can attach itself to the solid only at the edge of a step and as a result the crystal only grows by the passage of steps. The relationship between the

and the effective growth rate normal to the interface is umber and formation mechanism of new steps.

(ii) Uniform or continuous growth advances the interface without needing steps, that is, growth can equally well proceed from any point. For a given material and supercooling, it is important to determine which type of growth occurs.

The supercooling required for lateral growth at a given interface velocity, is typically much larger than that for continuous growth. Moreover, an interface that advances by continuous growth *can* propagate with a smoothly curved interface on a microscopic scale while lateral growth leads to facets. Whereas growth from the vapor or growth from supersaturated aqueous solutions is easily observed and usually occurs by lateral growth, such atomic scale observations are not usually possible for melt growth. Thus the nature of the S-L interface for metals is the subject of various models. In fact there is strong evidence that most metals freeze by continuous growth [2].

II. 3. PLANAR SOLIDIFICATION

The analysis of the shape of the **S-L** interface on a scale larger than atomic dimensions begins with a consideration of plane front growth. It is also important as a starting point to understand the more complex interface shapes involving cellular and dendrite growth. To achieve planar growth, it is necessary to obtain S-L interface that is both macroscopically and microscopically planar. The former is achieved by controlled directional solidification with good furnace design and avoiding convection in the melt. The latter is achieved by avoiding interface instabilities due to constitutional supercooling**.** [3]

II.3.1. Cellular Solidification

Under directional solidification conditions, a cellular or a cellular dendritic interface is observed when the interface velocity exceeds the critical velocity for the planar interface

the cellular structures that form have two important ell is small, and it is of the same order of magnitude as the cell spacing. Second, the tip region of the cell is broader, and the cell has a larger tip radius. At higher velocities, a cellular dendritic structure forms in which the length of the cell is much larger than the cell spacing. Also, the cell tip assumes a sharper, nearly parabolic shape, which is similar to the dendrite tip shape so that the term cellular dendritic is used to characterize this structure.

The formation of cellular structures gives rise to solute segregation in the solid. The tip of the cell is at a higher temperature than the base of the cell. Thus, for $k < 1$, the solid that forms at the cell tip will have a lower composition than the solid that forms at the cell base. This microsegregation profile is approximately characterized by the normal freeze, or Scheil, **Equation II.9**: [3]

$$C_S = k \cdot Co\,(1 - f_S)^{k\,\ddot{\imath}\,1} \qquad (\text{II.9})$$

Where f_S is the volume fraction of solid, which is 0 at the cell tip and 1 at the cell base. **Equation II.9** is derived under the assumptions that k is constant and that the composition of liquid is uniform in a small-volume element in the direction perpendicular to the growth direction. **Equation II.9** also assumes that the diffusion in the solid is negligible, so that it predicts C_S to be infinity at the base of the cell. **Equation II.9** is useful for nonequilibrium solidification when the phase diagram shows the presence of a higher composition second phase that can nucleate in the intercellular region. For example, for systems with eutectic phase diagrams, the maximum composition in the single phase corresponds to $k.C_E$, where C_E is the eutectic composition. [3]

II. 3. 2. Dendritic Solidification

A dendritic structure is formed when the interface velocity is increased beyond the cellular dendritic regime. Dendritic structures are characterized by the formation of sidebranches. These sidebranches, as well as the primary dendrite, grow in a preferred

, <100> for cubic metals, so that cubic metals exhibit onal view of dendrites in metals is difficult to observe because only parts of dendrites that intersect the plane of polish are visible.

The formation of secondary dendrite arms is clearly seen for a dendritic structure in a transparent alloy. The secondary arms form very close to the dendrite tip, and the first few sidebranches are uniformly spaced. However, the secondary arm spacing increases as the base of the dendrite is approached. Initial coarsening occurs by the competition in the growth process among secondary arms. However, once the diffusion fields of their tips interact with those of the neighboring dendrite, the growth of the secondary arms is reduced, and a coarsening process to reduce interfacial energy begins. The final secondary arm spacing near the dendrite base is significantly larger than that near the dendrite tip. This final secondary arm spacing controls the microsegregation profile in the solidified alloy. This microsegregation pattern is analogous to that discussed for the cellular structure, except that the periodicity of segregation is controlled by the final secondary arm spacing and not by the primary spacing.

The secondary dendrite arm spacing increases with the distance behind the tip. Because the secondary arm coarsening requires solute diffusion, the coarsening process is negligible once the interdendritic liquid has solidified. Thus, the final value of secondary spacing, λ_2 is determined by the total time that a given secondary branch spends in contact with the liquid because the diffusion coefficient of the solute is significantly larger in the liquid than in the solid. [3]

II.3.2.1. Primary Arm Spacing

Two simple relationships for the primary Dendrite Arm Spacing will be discussed here. The first relationship can be obtained based on *Flemings*. Ignoring solute diffusion in the x-direction, material balance dictates: [4]

$$\frac{C_L}{t} \qquad \text{(II.10)}$$

Where $\frac{dC_L}{dt} = \frac{dC}{dx}\frac{dx}{dt} = -\frac{V_y G_L}{m}$ Upon substitution in the governing equation:

Figure II.5 Phase-Field method simulation of a Ni -0.41 at traction Cu dendrite growing in an undercooled melt. [5]

$$\frac{d^2 C_L}{dy^2} = -\frac{V}{D_L}\frac{G}{m}$$

Integrating again between C_o/k and C_L^{max} (in the interdendritic spacing), and between 0 and $\lambda/2$ gives: [4]

$$\lambda_1 = ct(GV)^{1/2} \qquad or \qquad \lambda_1 = ct\left(\dot{T}\right)^{-n}$$

Examples of cooling rates and dendrite arm spacing are given in **Table II.1**

Table II.1 Range of cooling rates in solidification process [6]

Cooling Rate, K/s	Production Process	Dendrite arm spacing (μm)
10^{-4} to 10^{-2}	Large castings	5000 to 200
10^{-2} to 10^{3}	Small castings, continuous casting, die casting, strip casting, coarse powder atomization	200 to 5
10^{3} to 10^{9}	Fine powder atomization, melt spining, spray deposition, electron beam or laser surface melting	5 to 0.05

Kurz and Fisher (7) have derived a more complex relationship. Assume that the dendrites are half of ellipsoids of revolution **Figure II.6**

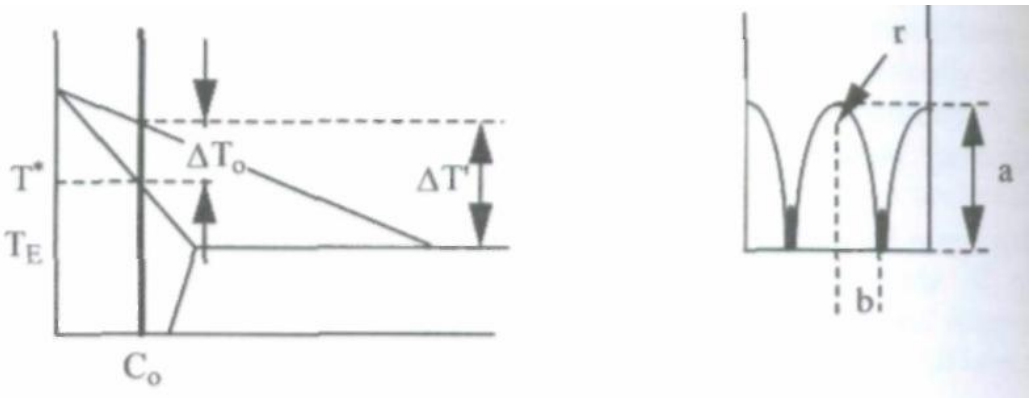

Figure II.6 Assumptions to calculating DAS. [7]

r = b^2/a. For a hexagonal arrangement of dendrites b = 0.58λ_1. From the phase diagram it can be approximated that:

$$a = \frac{\Delta T^1}{G} = \frac{T^* - T_E}{G} \approx \frac{\Delta T_0}{G}$$

This approximation is increasingly valid, as the composition of the alloy is closer to the eutectic. Then: $(0.58\lambda)^2 = r\Delta T_0/G$, or $\lambda_1 = (3\Delta T_0 r/G)^{1/2}$. Since $r = 2\Gamma/(D_L/(V\Delta T_0))^{1/2}$:

$$\lambda_1 = \mu_1 . V^{-4} . G^{-4} \quad where \quad \mu_1 = 4.3\left[\Delta T_o D_L \Gamma\right]^{1/4}$$

The constant refers to a single-phase alloy.

Earlier, *Hunt* (8) has derived a similar equation for primary spacing different only through the numerical constant, which was 2.83 rather than 4.3. Note that all models introduced here demonstrate that the primary spacing is a function of *G* and *V*. [3]

Bouchard and Kirkaldy (9) tested these equations against experimental data for steady-state solidification of cells (28 alloys) and dendrites (21 alloys) in binary alloys. The experimental data summarized by the following equations agree reasonable well with theoretical predictions: [9]

For cells $\lambda_1 = ct\left(\dot{T}\right)^{-0.36\pm0.05}$

For dendrites $\lambda_1 = ctV^{-0.28\pm0.04}G^{-0.42\pm0.04}$ *and* $\lambda_1 = ct\left(\dot{T}\right)^{-0.3\pm0.03}$

v all equations failed to perform adequately.

blished, it will remain constant throughout steady -state solidification, and during cooling in solid state. If non-steady state solidification occurs, the primary spacing will change. [4]

Recently Turkeli investigated primary arm spacing in carbon steels and compared with current primary arm models. He showed that prediction of the Hunt equation underestimates the experimental values whereas the Kurz-Fisher equation, Laxmananôs minimum undercooling and stability equations, Trivedi equation and Ma-Sahm equation overestimate them. He also modified Ma-Sahm equation and showed that this modified model can predict very closely experimental measurements and also many available experimental data in literature [10]

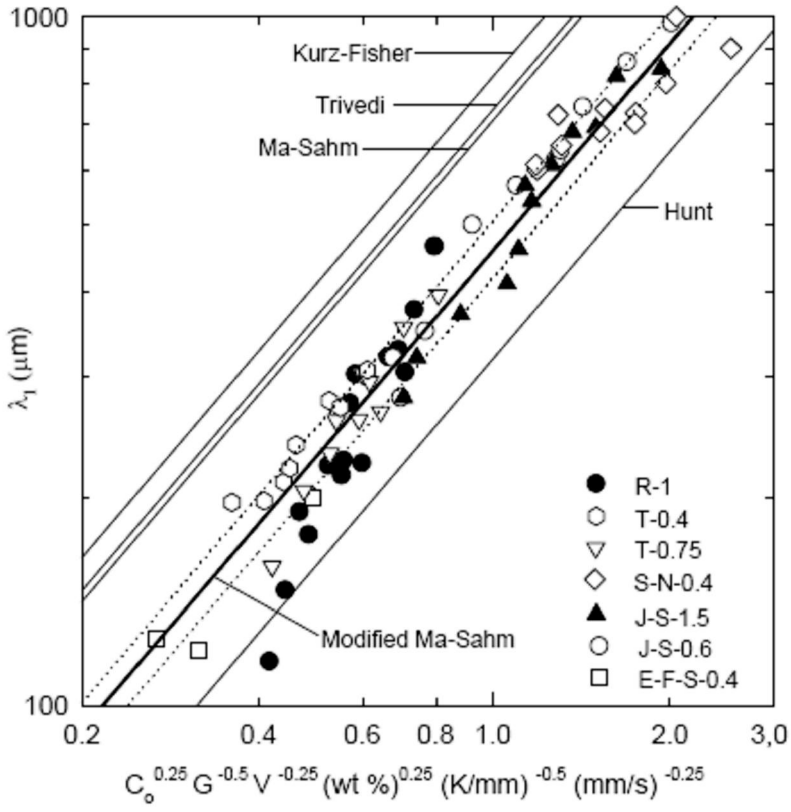

Figure II.7 Comparison between theoretical models and all experimental data for some kind of austenitic steels (regression line calculated due to 70 data is shown as a thick line) [10]

II.3.2.2. Secondary Arm Spacing

In the early understanding of dendrite growth, it was assumed that the secondary dendrite arm spacing is formed at the beginning of solidification. Then, arms thicken and grow as solidification proceeds. Thus, the final arm spacing, λ_f , was thought to be the same as the initial spacing, λ_0.

The smaller arms remelt (dissolve) and eventually disappear. Consequently, throughout solidification the DAS increases and $\lambda_f > \lambda_0$ as seen at **Figure II.8** [11]

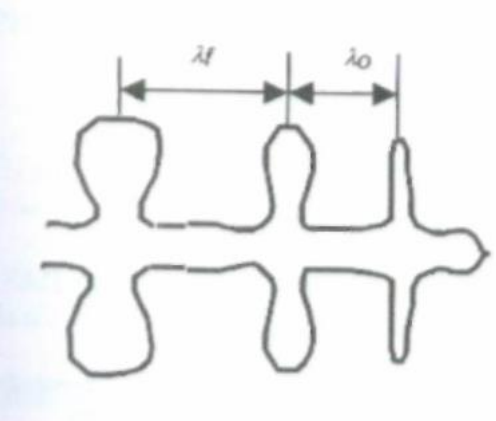

Figure II.8 Schematic drawing illustrating the increase of the secondary DAS. [11]

This is the dynamic coarsening of dendrites. The effect of coarsening on the secondary DAS of a transparent organic material is shown in **Figure II.9**

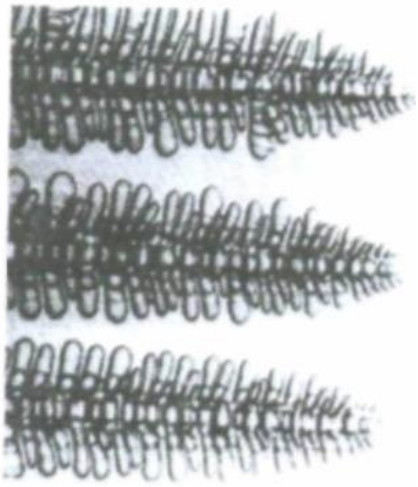

Figure II.9 Dendrite structure in succinonitrile. [11]

DAS increases with the distance behind the tip. Some typical coarsening mechanisms are shown in **Figure II.10** [11]

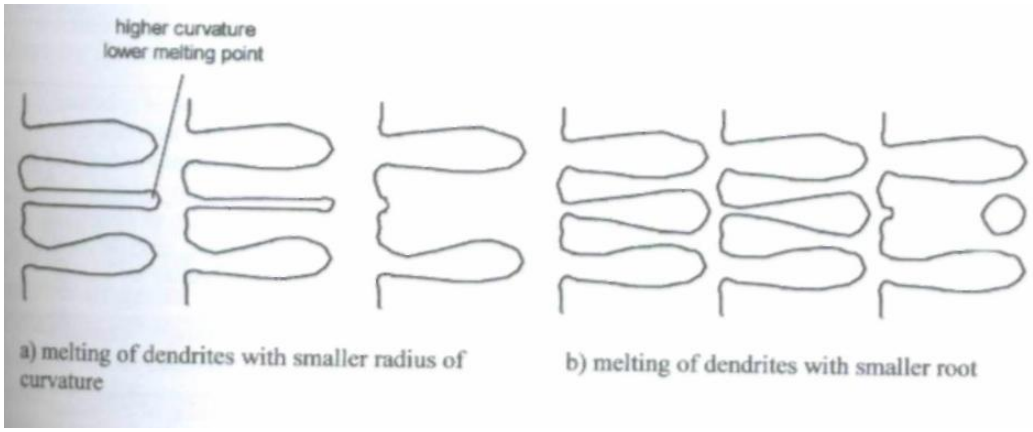

Figure II.10 Coarsening mechanisms [11]

Many mathematical models have been developed for dendrite coarsening based on the following concepts. Dendrite coarsening is diffusion-controlled, the diffusive species under consideration being the solvent. Assuming isothermal coarsening, the growth rate of the distance, ə; between two spherical particles must be proportional to the compositional gradient: [11]

$$d\lambda / dt = ct.(\Delta C_L / \lambda)$$

The liquid temperature and composition in equilibrium with a solid surface depends on the curvature of that surface. Indeed, the curvature undercooling at the tip of the dendrite is œ*T*, = 2Ţ/r. Since œ*T*, = *m* œC_r, œ C_r =2 Ţ *l* (*m r*) = *c t* . r $^{-1}$. Curvature and local curvature differences must increase approximately proportionally with the inverse of the spacing ə. Thus, *r* = *ct*. ə. It follows that œ*C*, = *ct*. ə$^{-1}$ and also: [11]

$$\Delta C_L = \Delta C_{r1} - \Delta C_{r2} = ct.\lambda^{-1}$$

n an initial arm spacing, ϑ₀ and final arm spacing ϑf and fication time (the difference between the times when the liquidus isotherm and the solidus isotherm pass the particular micro volume), t_f gives: [11]

$$\lambda_f^3 - \lambda_0^3 = \mu_0 . t_f$$

Assuming that ϑ₀<< ϑf= ϑ₂ results in a final secondary arm spacing of:

$$\lambda_2 = \mu_0 . t_f^{1/3}$$

Where t_f is the local solidification time.

Using the experimental data presented **Figure II.11** it can be calculated that, for *AV* 4.5% *Cu* alloys; the constant in the coarsening law has a value of 10^{-6} m/s^3.

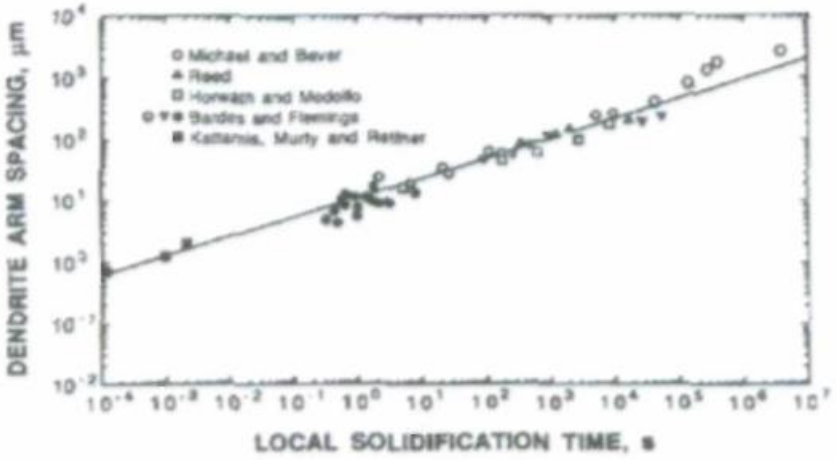

Figure II.11 Relation between DAS and solidification time for Al-4.5% Cu Alloys [11]

The constant has been derived by a number of authors, mostly for the case of spherical particles (see for example derivation in inset). Some typical formulations and their basic assumptions are given in **Table II.2** Isothermal coarsening means that the only driving force is solute diffusion (f_s = constant). However, during solidification the temperature decreases, f_s

ce, thermal diffusion, must be considered. This is

Table II.2 Coarsening constants [11]

Model	Coarsening constant	Basic assumptions
Kattamis-Flemings, 1965	$\mu_o = \frac{20 D_L \Gamma \ln(C_E/C_o)}{m_L C_L (k-1)(C_E - C_o)}$	isothermal coarsening, of spheres; see inset for derivation
Ardell, 1972	$\mu_o = \frac{v_m^2 \gamma_{SL} C_o D_L}{RT}(1-C_o)\frac{1-f}{f}$	dynamic coarsening of spheres, diffusion of solute depends on a characteristic distance defined by the main free path
Voorhes-Glicksman, 1984	$\mu_o = \frac{8}{9}\frac{v_m^2 \gamma_{SL} C_o D_L}{RT}\frac{\alpha^3}{1-f^{1/3}}$ α: fct. of f_S given in tabulated form	solution of dynamic multiparticle diffusion problem; random pattern of precipitates generated by Monte Carlo simulation
Mortensen, 1991	$\mu_o = \frac{27 D_L \Gamma}{2 m_L C_L (k-1) f_S^{2/3}(1-f_S^{1/3})}$	dynamic coarsening of spheres
	$\mu_o = \frac{27 D_L \Gamma}{4 m_L C_L (k-1) f_S (1-f_S^{1/2})}$	dynamic coarsening of cylinders

II.4. COLUMNAR STRUCTURES

Most commercial alloys exhibit a much more highly branched morphology similar to the transparent organic alloy. **Figure II.12** is a drawing of a portion of a dendrite from one such material, low-alloy steel. The figure was drawn from a three-dimensional study of isoconcentration surfaces of a steel dendrite after complete solidification. The contour lines approximately represent successive portions of the liquid-solid interface. An important aspect of the sketch of **Figure II.12** is that spaces between dendrite arms tend to fill in during the

ıtes. These plates produce some rather surprising effects

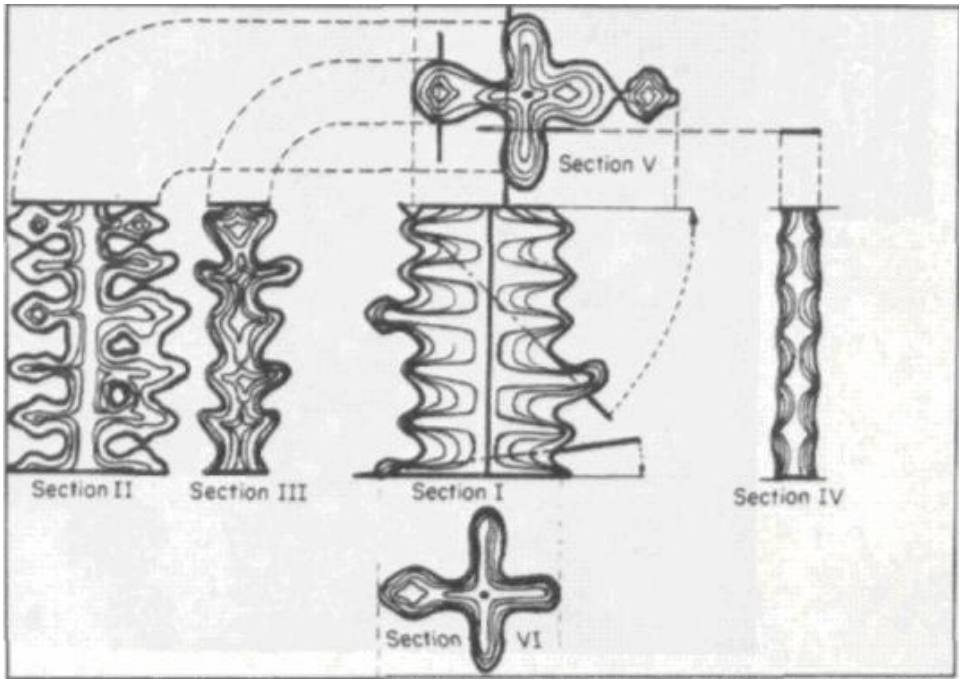

Figure II.12 Isoconcentration surfaces of a columnar dendrite, low alloy steel. [4]

Low-alloy steel has a particular advantage for the study of dendrites in that it is possible to heat-treat it so that the low-alloy central portions of the dendrite transform to pearlite while the outer portions are quenched to martensite. The boundary between the pearlite and martensite then represents an isoconcentration surface, and the heat treatment can be modified to delineate isoconcentration surfaces of higher or lower magnitude. [4]

The *plates* observe in columnar structures often extend over many primary dendrite arms. In **Figure II.12** note how well aligned the dendrite arms are along a direction about 20^0 from the horizontal. The degree to which dendrites show a platelike structure in columnar solidification depends on alloy composition. Alloys which freeze with only a minor fraction of eutectic usually show pronounced plates. On the other hand, alloys in which a relatively large fraction of the solid forms as eutectic usually have much less well ï developed plates. Dendritic structures in noncubic metals are more complex geometrically than those discussed above because of nonorthogonality of dendrite arms. [4]

II.5. EQUIAXED GRAINS

It was once assumed that each crystal in a casting or ingot represented a new nucleation event. Perhaps this is true in castings in which a strong nucleating agent is present. However, it has now been amply demonstrated that *grain multiplication* is an important and general source of crystals in castings and ingots. [4]

If the arm that is separated is then carried away into slightly supercooled liquid, a new crystal is formed without an added nucleation event. Convection provides an admirable mechanism, not just for carrying away the dendrite arm, but also for dissipating superheat in the liquid so that transported arm, but also can grow when reaching it. Also, turbulent convection has added effect of bringing heat pulses to the interface. These heat pulses accelerate the melting off of dendrites. [12-14]

When this convection is reduced, grain size is larger and columnar structures are much more readily obtained. Convection appears to play a dominant role in formation of the outer *chill* zone as well as in the columnar-equiaxed transition. When convection is absent, no outer chill zone is observed even though rates of heat extraction may be very high indeed.

It has been suggested that the roots of secondary dendrite arms may have a slightly higher solute content than outer portions of the arms. Thus, the malting point here would be lower, and thermal fluctuations would tend to cause melting just at the location. In any case, the roots of dendrite arms are often smaller diameter than exterior portions, and even if melting in response to the arm from fluctuation were uniform, it would result in separation of the arm from the main stalk. It has also been suggested that mechanical fracture resulting from the stress caused by fluid flow might be enough to lead grain multiplication, but there is no experimental verification that this mechanism operates. [12-14]

There have been few detailed structural studies of equiaxed dendrites, although many examples of etched structures are to be found in the foundry literature and in textbooks on metallography. Some examples of different types of structures are shown in **Figures II.13** and **II.14**[4]

Generally, coarse grained equiaxed structures show dendrites described earlier, except that there is little, if any, preferential orientation in the heat-flow direction. Plates are often evident except in alloys which contain a relatively large amount of eutectic. As grain size is

e dendrite arm spacing, the dendrite arm spacing, the llographic appearance and more second phase is found at grain boundaries than in interdendritic regions. [4]

When, at the limit, grain refinement is so effective that a dendritic structure can not from or at least cannot survive the initial stages of solidification, the final structure is as in **Figure II.14/b**, with spherical morphology of isconcentrates within each grain. The minimum grain size that can be obtained in these *nondetuiritic* alloys is determined by coarsening kinetics in the same way as in secondary dendrite arm spacing in dendritic alloys. Unfortunately, highly refined nondendritic structures such as that of **Figure II.14/b** have been obtained in very few alloys, the only important commercial example being zirconium-refined magnesium alloys. The limited data available show little difference in microsegregation between columnar are equiaxed grains, as would be excepted from the simple analysis described earlier. When differences are found, there is usually more segregation in the equiaxed region. One possible reason for this is interdendritic fluid flow. [4]

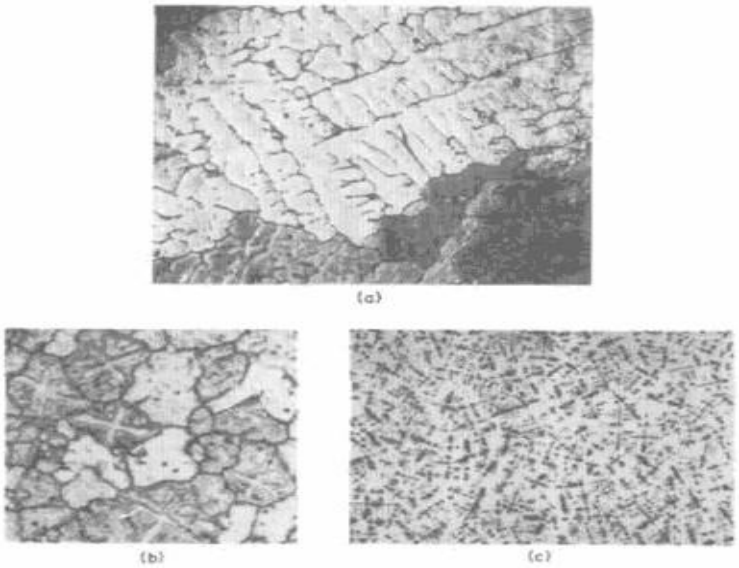

Figures II.13 Some equiaxed dendritic structures. (a) A1-4,5%Cu alloy (magnification x75) (b) high-strength grain refined aluminum alloy (magnification x75);(c) Fe-25% Ni alloy (magnification x12) [4]

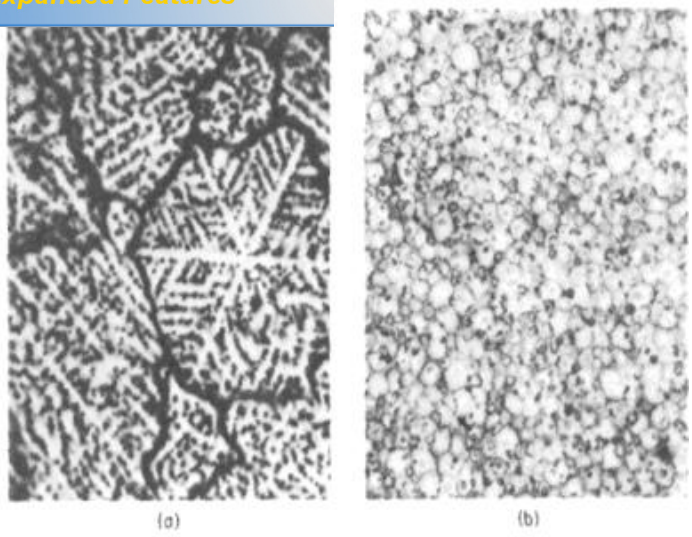

Figures II.14.Magnesium-zinc alloy (magnification x55). (a) Not grain refined; (b) grain Refined by zirconium addition.(From Kattamis et al.[3.3.]) [14]

PART III

MICROSEGREGATION

III.1. MICROSEGREGATION

All metallic materials contain solute elements or impurities that are randomly distributed during solidification. The variable distribution of chemical composition on the microscopic level in a microstructure, such as dendrites and grains, is referred to as microsegregation. On the other hand, variation on the macroscopic level is called macrosegregation. Because these segregations generally deteriorate the physical and chemical properties of materials, they should be kept to a minimum.[15]

In practice, microsegregation is usually evaluated by the Microsegregation Ratio, which is the ratio of the maximum solute composition to the minimum solute composition after solidification, or by the amount of non-equilibrium second phase in the case of alloys that form eutectic compounds. Some data and an isoconcentration profile for an Fe-25Cr-19Ni columnar dendrite are given **Figure III.1** [15]

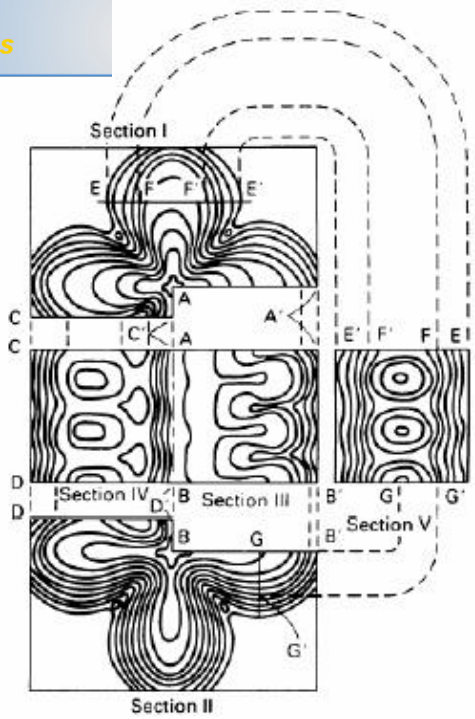

Figure III.1 Isoconcentration profile in an Fe-25Cr-20Ni columnar dendrite.[15]

III.1.1. Equilibrium Solidification

Since the composition of the liquid and solid have been proven to be different, which means simply that chemical diffusion will be active during and after solidification, it is important to explore its effects, resulting in solute redistribution. The final composition in a solidifying casting, assuming only diffusive transport, depends on the liquid and solid diffusivity, and on the partition coefficient (k). [11]

Analysis of solute redistribution during directional solidification can be conducted on the basis of the following assumptions: [11]

1. Equilibrium Solidification

2. Non-Equilibrium Solidification

2. a. No diffusion in solid, complete diffusion in liquid

2. b. No diffusion in solid, limited diffusion in liquid

omplete diffusion in liquid

2. d. Limited diffusion in solid and liquid

2. e. No diffusion in solid, partial mixing in liquid

2. f. . No diffusion in solid, complete diffusion in liquid and dendrite arm coarsening

Firstly, we will examine Equilibrium solidification. In Equilibrium solidification, It is assumed that the solute can completely diffuse in the solid ($D_S = \infty$) and in the liquid $\left(D_L = \infty\right)$.

The solute elements in alloys are redistributed during the solidification process so that the chemical potential in the liquid and solid phases is equalized. As the solidification proceeds under the equilibrium condition, the solute compositions in the solid, C_s, and the liquid, C_L, vary along the solidus and liquidus lines, respectively **Figure III.2** The ratio C_s/C_L is referred to as the equilibrium partition or distribution coefficient, k. [15]

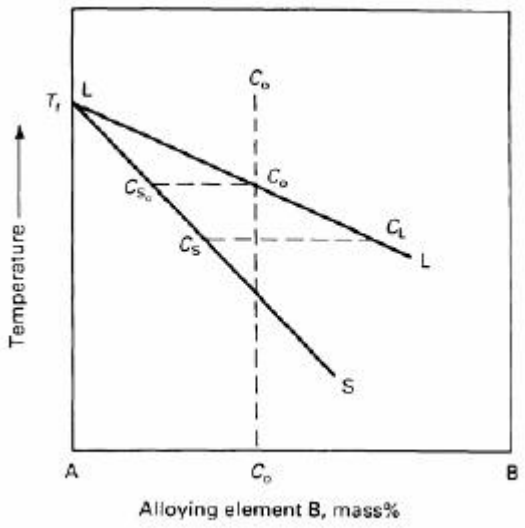

Figure III.2 Schematic of an equilibrium phase diagram of a binary alloy. The liquidus is represented by line LL; the solidus by line LS. [15]

In the equilibrium condition, the liquid and solid composition can be calculated by **Equation III.1.**

$$C_s = \frac{kC_0}{1-(1-k)f_s} \qquad \text{(III.1)}$$

where Co is the initial alloy composition and f_s is the solid fraction, and by:[15]

$$C_s = k\, C_L \qquad \text{(III.2.)}$$

After solidification (f_s = 1), the solute composition is designated *C*o; theoretically, no microsegregation occurs at this point. In actuality, however, the equilibrium solidification rarely takes place, because the solute diffusion is not so rapid. [15]

As known, another expression type of equilibrium solidification has that the assumption is equivalent to the case of equilibrium solidification, where either enough time is available for the solid- and liquid-solutions to become completely homogeneous from the chemical standpoint (Vs→ 0), or diffusion is very rapid in both the solid and the liquid. As solidification proceeds under equilibrium conditions, the solute composition in the solid, C_S, and in the liquid, C_L, vary along the solidus and the liquidus line of the phase diagram, respectively **Figure III.3**. [16]

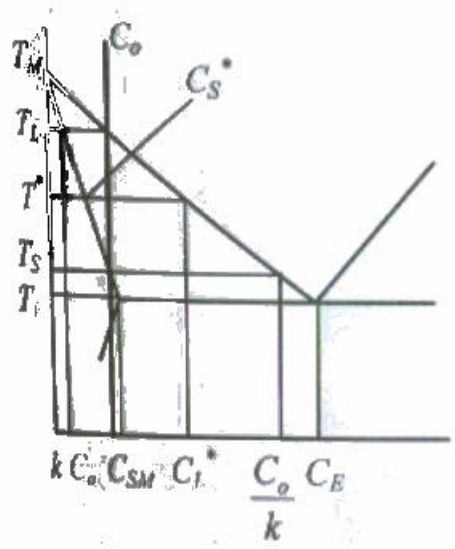

Figure III. 3. Schematic Phase Diagram [11].

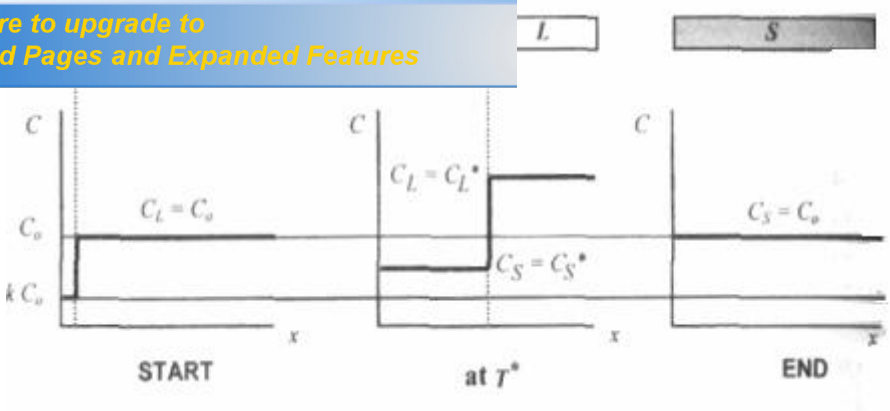

Figure III.4 Equilibrium Solute Redistribution in a Unidirectionally Solidified Casting [11].

Figure III.4 shows the composition profile of the solute in the solid and in the liquid, in a unidirectionally solidified sample, at three different stages: immediately after the beginning of solidification, at an intermediate time, and at the end of solidification. The initial composition of the alloy is C_0, i.e., the alloy contains C_0 % solute. Thus the liquid composition at the beginning of solidification is $C_L = C_0$. As imposed by the partition coefficient, k, the first amount of solid to form will have the composition $C_S = k\ C_O$,. This means that the solid will have less solute than the liquid, and thus the solid will reject some solute when it solidifies. [16]

At an intermediate time during solidification, when the interface temperature is T^*, the composition of the liquid has risen to $C_L^* > C_0$ and that of the solid to $C_s^* > kC_0$. [16]

Writing a material balance (conservation of solute atoms) at T *gives: [11]

$$C_s f_s + C_L f_s = C_0 \qquad \text{with} \qquad f_s + f_L = 1 \tag{III.3}$$

where f_s and f_L are the mass fraction of solid and the fraction of liquid respectively. Knowing that $C_S = k\ C_L$, the composition of solid is calculated to be: [11]

$$C_s = \frac{kC_0}{1-(1-k)f_s} \tag{III.4}$$

This equation is called the equilibrium lever rule. It is valid assuming $\rho_S = \rho_L$. [11]

At the end of solidification, because of rapid solid diffusion, the composition of the solid is uniform across the volume element, and equal to the initial composition of the liquid. Note that in spite of the equilibrium nature of solidification, substantial solute redistribution occurs during solidification. The material is homogeneous only before and after solidification. [11]

For the more general case, when $\rho_S \neq \rho_L$ a similar equation can be obtained by using volume fractions, g_s and g_L rather than mass fractions. Then, when substituting f_S with $g_s \rho_s / \rho$ in Equation 2.4, the equilibrium lever rule becomes: [11]

$$C_s \frac{1-(1-\rho_s/\rho_L)g_s}{1-(1-k\rho_s/\rho_L)g_s} kC_0 \qquad \text{(III.5)}$$

Note that, if $\rho_S = \rho_L$, this equation reduces to the previous one.

III.1.2. Non-Equilibrium Solidification

If the solute redistribution in a volume element between plate like dendrites as shown in **Figure III.5** is considered and if negligible undercooling at the solid/liquid interface (local equilibrium condition) with no net flow of solute through the volume element is assumed, the liquid composition can be calculated [15].

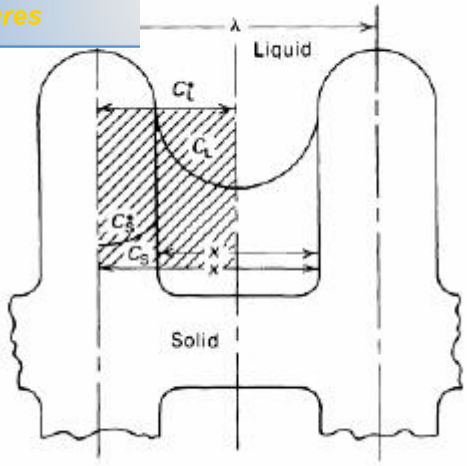

Figure III.5 Solute distribution in a volume element (crosshatched area) between dendrites [15].

III.1.2.1. No diffusion in solid, Complete Diffusion in Liquid (The *Gulliver-Scheil* Model)

The basic assumption is that diffusion is very rapid ($D_L=\infty$), or there is complete mixing (convection) in the liquid, but there is no diffusion in the solid (D_S = *0)*. The graphical representation of this case is given in **Figure III.6** Note that since complete mixing in the liquid is assumed there is no diffusion boundary layer ahead of the solidifying interface.

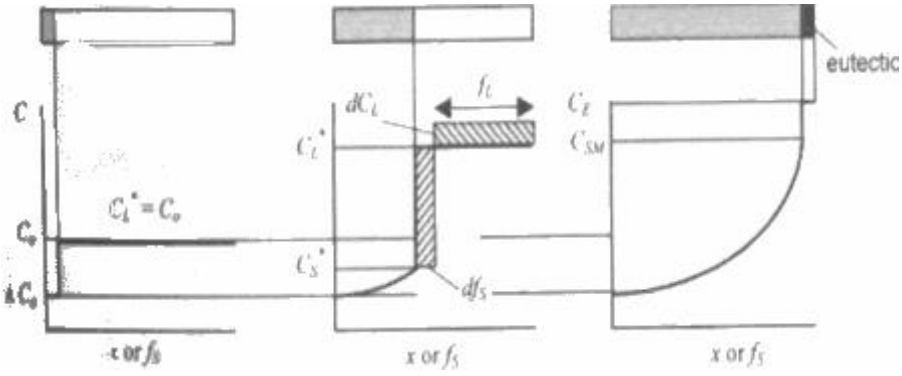

Figure III. 6 Solute Redistribution for Non-Equilibrium Solidification for $D_S = 0$ and $D_L=\infty$ [11]

At the beginning of solidification, the situation is identical with that for equilibrium solidification. Then, since there is no diffusion in the solid, a concentration gradient will be established between the initial solid composition kC_0 and the solid composition at the intermediate time (or temperature, T*), which is Cs*. In the liquid, the composition is

ince diffusion is very rapid. The composition of the solid dification, and will finally reach the maximum solubility in the solid solution, C_{SM}. [11]

To find an equation for the solid composition as a function of the solid fraction, material balance equations must be used. In the original derivation by Gulliver (1913) and Scheil (1942) a material balance at the interface was written: [11]

Solute rejected when df_s is formed = solute increase in liquid

That is: [11]

$$(C_{*L} - C_S^*)df_s = (1 - f_s)dC_L \qquad \text{(III.6)}$$

Since $C_L = C_S/k$, and $dC_L = dC_S/k$, on integration this equation becomes: [11]

$$\int_0^{f_s} \frac{df_s}{1-f_s} = \frac{1}{1-k}\int_{kC_0}^{C_s} \frac{dC_s}{C_s} \qquad \text{Or} \qquad C_s = kC_0(1-f_s)^{k-1} \qquad \text{(III.7)}$$

This is known as the Scheil (more recently Gulliver-Scheil) equation, or the non-equilibrium lever rule. Note that, for $f_s = 1$, $C_s = \infty$. This is not true for alloy solidification. The composition of the solid can only increase to the maximum solid solubility, C_{SM} , and that of the liquid to the eutectic composition, C_E. As solidification proceeds, the solid composition follows the solidus line from kC_0 to C_{SM} and then to C_E, **Figure III.3** The Gulliver-Scheil equation can also be derived from overall mass balance. [11]

III.1.2.2.No Diffusion in Solid, Limited Diffusion in Liquid

The basic assumptions are: Ds= 0 and $0 < D_L < \infty$. Solute redistribution for this case is shown in **Figure III.7**. A diffusion layer will exist ahead of the interface, and equations that are more

quid and solid composition. Three distinctive zones are

I: The initial transient, between T_L and T_S: Because of the boundary layer

II: The steady state, at T_S

III: The final transient, between T_S *a*nd T_E*:* Build up of solute occurs because the boundary layer reaches the end of the crucible.

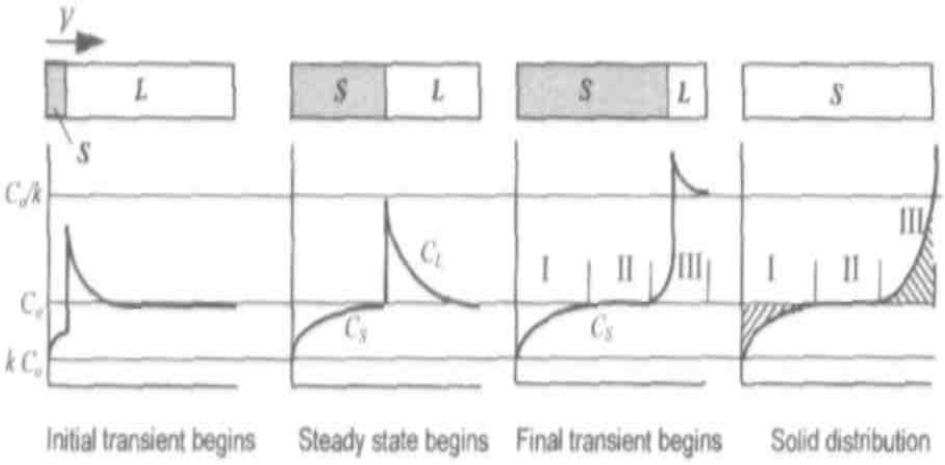

Figure III.7 Solute Redistribution for Non-Equilibrium Solidification for D_s= and $0 < D_L < \infty$. [11]

The initial and final transient represents chemical segregation. The shaded areas in **Figure III.7** must be equal to conserve mass balance, so that the average composition remains C_0. Calculation of solute redistribution during the initial transient can be done by using the time dependent form of the relevant diffusion Equation. The solution of this equation is: [11]

$$C_s = C_0\left[1-(1-k)\exp(-k\frac{V}{D}x)\right] \qquad \text{(III.8)}$$

Alternatively, solute flux balance can be used to derive the equation for the initial transient.[11]

During steady state solidification, the planar S/L interface grows at T_S. The composition of the liquid at the interface is $C_L^* = C_0 / k$ and then decreases according to **Equation III.9,** and reaches C_0 after a distance of approximately $2D_1 / V$. [11]

$$\left.\exp\left(-\frac{Vx}{D_L}\right)\right] \qquad \text{(III.9.)}$$

Steady state exists as long as there is enough liquid ahead of the interface for the forward diffusion of the solute to occur, and as long as solidification velocity remains constant. As the boundary of the sample is approached the first condition is not fulfilled anymore and solute content increases above C_0 **Figure III.8**. This is the final transient. The length of the final transient is that of the solute boundary layer, D_1 / V . [11]

The research group Smith et al. derived that the solid composition in the final transient can be calculated with: [2]

$$\frac{C_S}{C_0} = 1 + 3\frac{1-k}{1+k}\exp\left(-\frac{2Vx}{D}\right) + 5\frac{(1-k)(2-k)}{(1+k)(2+k)}\exp\left(-\frac{6Vx}{D}\right) + \\ + \ldots\ldots + (2n+1)\frac{(1-k)(2-k)\ldots(n-k)}{(1+k)(2+k)\ldots(n+k)}\exp\left[-\frac{n(n+1)Vx}{D}\right] \qquad \text{(III.10)}$$

where x=0 at the end of the specimen.

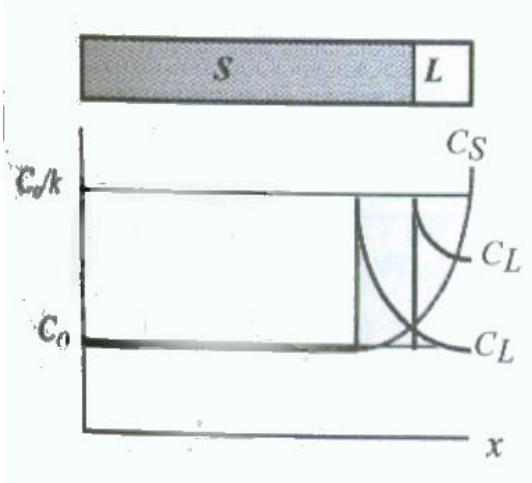

Figure III.8 Solute accumulation during the final transient. [11]

So far, it was assumed that the solidification velocity is constant during solidification. However, this condition does not hold in most solidification processes. Notable exceptions are directional solidification and crystal growth. If the solidification velocity V is suddenly increased $(V \rangle V_0)$ the diffusion layer decreases, which means that the amount of solute transported forward decreases. Conservation of solute atoms requires then an increase in the

ch in solute (positive segregation) is formed, as shown

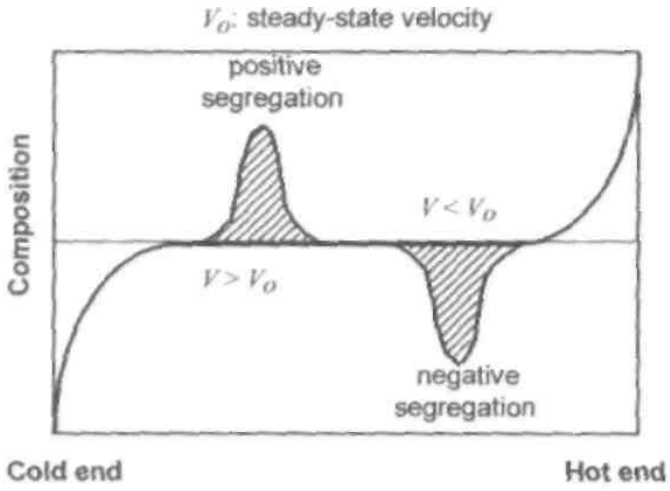

Figure III.9 Formation of positive and negative segregation when solidification velocity is different from steady state velocity. [11]

On the contrary, when the solidification velocity is suddenly decreased $(V \rangle V_0)$, a band poor in solute (negative segregation) is formed. If V or δ_C varies periodically, then periodical composition changes are produced. They are called banding. [11]

III.1.2.3. Partial (Back) Diffusion in Solid, Complete Diffusion in Liquid

This model attempted to describe this problem was proposed by *Brody* and *Flemings* (1966). The basic assumptions of the model included $D_S \rangle 0$, $D_L \to \infty$, and some back-diffusion of solute in the solid occurs at the interface. To solve the mass balance equation in additional assumption was necessary, *i.e.*, *V*=ct. Two cases can be considered: [11]

- linear growth: $f_S = t / t_f = x / l$
- parabolic growth: $f_S = \sqrt{t / t_f}$

where t_f is the final solidification time. Unidirectional solidification typically imposes linear growth in the specimen. Solidification of dendrites is commonly assumed to follow parabolic growth. [11]

$$C_S = kC_0\left(1-\frac{f_S}{1+k\alpha}\right)^{k-1} \qquad \text{(III.11)}$$

For parabolic growth the equation is (see inset for derivation): [4]

$$C_S = kC_0\left[1-(1-2\alpha k)f_s\right]^{\frac{k-1}{1-2\alpha k}} \qquad \text{(III.12)}$$

In these equations α is the dimensionless back-diffusion coefficient, calculated as: [4]

$$\alpha = \frac{D_S t_f}{l^2} \qquad \text{(III.13)}$$

Equations III.11 and.12 have been obtained without solving the ñFickianò diffusion. Because of that, when significant solid-state diffusion occurs, mass balance is violated. This can be understood by examining by **Figure III.10 and 11**. Mass balance for the boundary layer δ_S is correctly described by the equation given for A_3 only as long as the boundary layer is smaller than the solidified region. Consequently, the application of these equations is limited to slow diffusion when the boundary layer is small. [11]

Another problem is to solutal profile shown in **Figure III.10**. If diffusion in solid is finite, the solutal profile should be intermediate between that predicted by Scheil and equilibrium, as shown in **Figure III.12** C_s^* should decrease which in turn will determine a lower C_L^*.[11]

Indeed, in **Equation III.11** for $\alpha = 0$ we have $l^2 \rangle\rangle D_S\, t_f$ and this equation reduces to the Scheil equation. However, for the equilibrium condition which is $\alpha = \infty$, $l^2 \rangle\rangle D_S\, t_f$. This gives $C_S = kC_0$, which is the interface equilibrium condition but not the equation for equilibrium solidification. Similarly, **Equation III.12** reduces to the Scheil equation for

for $\alpha = 0{,}5$. Unfortunately, $\alpha = 0{,}5$ does not describe

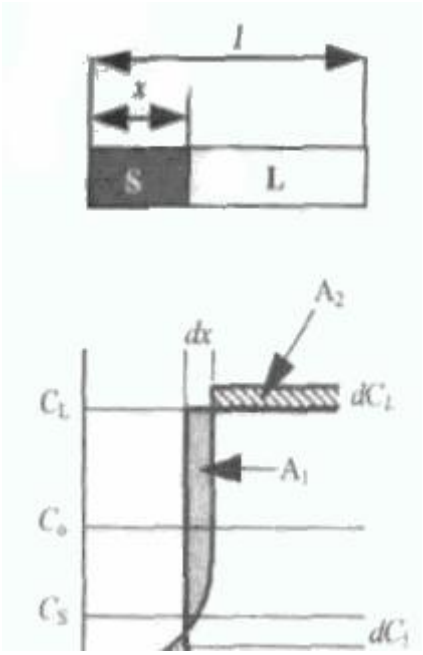

Figure III.10 Mass balance at the interface when complete diffusion in liquid and partial diffusion in solid are assumed. [11]

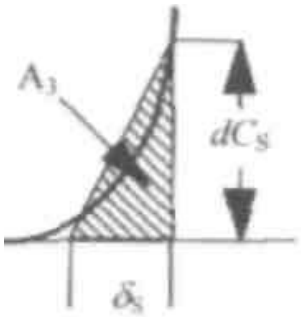

Figure III.11 Approximation for evaluation of solute back diffused in the solid. [11]

Clyne and Kurtz have used the Broody-Flemings model and added a spline fit to match prediction by Scheil equation and the equilibrium equation for the infinitesimal and infinite diffusion coefficient, respectively. The relation has no physical basis. [11]

Kobayashi (1988) obtained an exact solution (Laguarre polynomial). Solidification rate and physical properties were considered constant. Parabolic solidification was assumed for the planar geometry. A large number of terms (20,000 for a Fo = 0.05) is required for convergence. However, calculations with second order approximate solution were very close to the exact solution. This approximation is: [11]

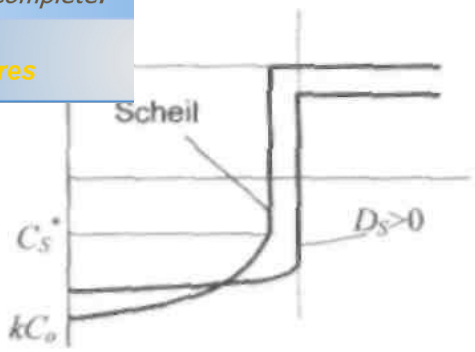

Figure III.12 Comparison between Scheil and finite diffusion in solid profiles. [11]

$$C_S = kC_0\xi^{\frac{k-1}{1-\beta k}}\left\{1+\Gamma\left[\frac{1}{2}+\left(\xi^{-2}-1\right)-2\left(\xi^{-1}-1\right)\ln\xi\right]\right\} \qquad \text{(III.14)}$$

where $y = 2\alpha$ for planar geometry and: [11]

$$\xi = 1-(1-\beta k)f_S \qquad \beta = \frac{2y}{1+2y}$$

$$\Gamma = \beta^3 k(k-1)[(1+\beta)k-2](4y)^{-1}(1-\beta k)^{-3}$$

Note that, for $D_S=0$ we have $y=0$, $\beta = 0, \Gamma = 0$ and $\xi = 1-f_S$ and this equation reduces to the Scheil equation. In addition, for $D_S \to \infty$ and $C_S = kC_0$, which upon integration gives equilibrium compositions. Kobayashi has also demonstrated that the Brody-Flemings and Clyne-Kurtz solution underestimate segregation by overestimating the effect of D_S, and are particularly inaccurate for low values of k and α .[11]

Before approximately decade, Himemiya and Umela (1998) developed an integral profile method that can consider all significant diffusion cases. For the case of finite diffusion in solid and complete diffusion in liquid, a second order differential equation was obtained. [2]

For linear growth the equation is: [11]

$$f_S^2(1-f_S)\frac{d^2C_L}{df_S^2}+\left[(k-4)f_{S+}^2(3k\alpha+3\alpha+2)f_S+3\alpha\right]\frac{dC_L}{df_S}=(1-k)(2+3\alpha)C_LC_0$$

1]

$$f_S^2(1-f_S)\frac{d^2C_L}{df_S^2}+[(k-4-6\alpha)f_S+(3k\alpha+6\alpha+2)]\frac{dC_L}{df_S}=(1-k)(2+6\alpha)C_LC_0$$

The Runge-Kuta method was used to solve these equations. [11]

III.1.2.4. Limited Diffusion in Solid and Liquid

In this case of $D_s = 0$ (finite diffusion in the solid) and D_L = Đ, **Equations III.15, 16, and 17** have been proposed:[11]

$$\frac{C_L}{C_0}=(1-\psi f_s)^{(k-1)/\psi} \qquad \text{(III.15)}$$

where

$$\psi \equiv 1-\frac{2Bk}{1+2B} \qquad \text{(III.16)}$$

where B is the back diffusion coefficient in the solid phase

$$B=\frac{4D_s t_f}{\lambda^2} \qquad \text{(III.17)}$$

Where D_s is the diffusion coefficient in the solid phase, t_f is the local solidification time, and ∂ is the dendrite arm spacing. A more accurate or exact solution for this model has been obtained. **Equation III.15** approximates the exact solution below $f_s < 0.9$. **Equation III.15** is applicable not only to plate like dendrites but also to columnar dendrites if 2B in **Equation III.16** is doubled. It also agrees with **Equation III.17** for D_S or B=1 and with **Equation III.17** for D_s or $B = 1$, respectively. The Brody-Flemings equation is not applicable for B > 0.5. [15]

The Himemiya-Umela model is applicable to this problem. However, complicated equations describing an initial value problem must be solved. A simple analytical model proposed by Nastac and Stefanescu is only valid at the micro-scale because of some of the assumptions made during derivation.[11]

rtial Mixing in Liquid

First, in the case of $D_S = 0$ and $D_L = \infty$ (indicating no diffusion in the solid and complete mixing in the liquid), where D_s is the solid diffusivity and D_L is the liquid diffusivity, **Equation III.18**, which is often called Scheil's equation, holds for any solid morphology:[15]

$$\frac{C_L}{C_0} = (1 - f_s)^{(k-1)} \qquad \text{(III.18)}$$

The segregation measured in solids is, in most cases, intermediate between that for complete mixing and no mixing. When a temperature gradient exists in the liquid, thermal convection will occur, because of the difference in destiny between the cold and hot metal. Therefore, mass transport is not only diffusion but also by fluid flow. A more complicated situation must be considered, and an additional assumption in necessary. [11]

As we known, within the diffusion layer of thickness δ **Figure III.13**, mass transport is by diffusion only, while outside it convection insures homogeneity within the liquid. In terms of hydrodynamics, the diffusion layer is stagnant. The diffusion layer is treated by using an effective distribution coefficient, k_{ef}. It can be shown boundary layer theory that k_{ef} is related to k by the equation: [11]

$$k_{ef} = \frac{k}{k + (1-k)\exp(V\delta / D_L)} \qquad \text{with} \quad 1 \le k_{ef} \ge k \qquad \text{(III.19)}$$

An equation similar to **Equation III.1** is derived for the calculation of the solid composition as a function of fraction of solid: [11]

$$C_S = k_{ef} C_o (1 - f_s)^{k_{ef}-1} \qquad \text{(III.20)}$$

Note that or $D_L \to \infty$, $k_{ef} = k$, and the equation for complete mixing (Scheil) is obtained. For $D_L \to 0$, $k_{ef} = 1$, $C_S = C_o$, which means that no mass transport occurs. [11]

of the various solute redistribution analytical model **gure III.13**. Note that complete mixing (Scheil model) occurs when considerable convection exists in the liquid. This is the case for most directional solidification experiments performed in the earthôs gravitational field. For experiments conducted in a micro-gravity environment the no-mixing gives a more realistic description of reality. [11]

It must be noted that, when using analytical models to evaluate segregation, it must be assumed that all physical properties are constant. The solid-state concentration can only be calculated at the interface, and can not be modified by subsequent solid diffusion. Many other analytical and numerical models have been proposed. Some of them will be reviewed as part of the discussion on micro-segregation. [11]

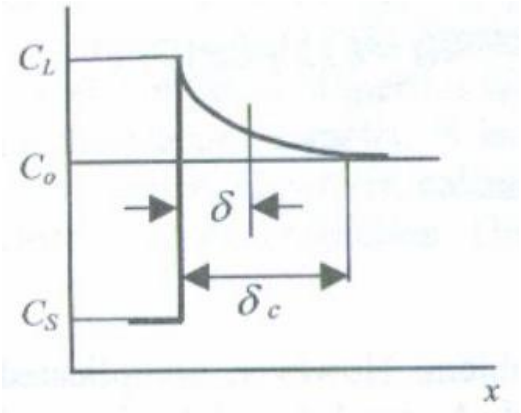

Figure III.13 Boundary layer when convection in the liquid is assumed. [11]

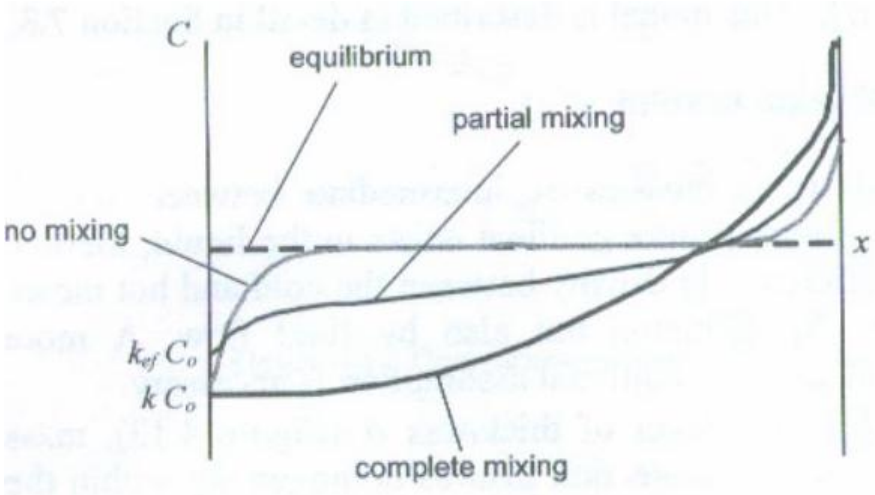

Figure III.14 Summary of solute redistribution. [11]

of solid-state concentration can be plotted. Thus, the e solid concentration across the whole length as well as at the interface, while the Brody-Flemings and the Kobayashi models, and can only calculate the interface solid composition.[11]

III.1.2.6. No diffusion in solid, complete diffusion in liquid and dendrite arm coarsening

In this model, it is assumed that the interdendritic liquid concentration changes as a function of time, starting from the average composition, C_O, and ending at the maximum composition, C_{Max} as follows:[16]

$$C_L = C_O + (C_{Max} - C_O)\left(\frac{t}{t_f}\right)^M \qquad \text{(III.21)}$$

M is constant and depends on partition coefficient, k, and coarsening exponent, n. It is also assumed that dendrite arms coarsen with time due to the power law equation:

$$L = At^m. \qquad \text{(III.22)}$$

In this equation, A and n are constants and can be determined by experimental methods in the quenched specimen during solidification or the prediction of theoretical models for A and n can be used, if there is no reliable data for any alloy.
The partial differential equation of Kirkwood without back diffusion in solid can be written as follows:

$$(C_L - C_S)\frac{dx_i}{dt} = (L - X_i)\frac{dC_L}{dt} + (C_L - C_O)\frac{dL}{dt} \qquad \text{(III.23)}$$

divided by L, noting $df_S=(dx_i/L)$ and $f_S=X_i/L$ then

$$(C_L - C_S)\frac{df_S}{dt} = (1 - f_S)\frac{dC_L}{dt} + (C_L - C_O)\frac{1}{L}\frac{dL}{dt} \qquad \text{(III.24)}$$

Differentiating the coarsening **Equation III.2** with time and replacing the $(C_L\text{-}C_O)$ term in **Equation III 24** with **Equation III 21** the last term of **Equation III 24** becomes:

$$\frac{d_L}{dt} = Ant^{n-1} \qquad \text{(III.25)}$$

$$(C_L - C_O)\frac{1}{L}\frac{dL}{dt} = (C_{Max} - C_O)\left(\frac{t}{t_f}\right)^M \frac{n}{t} \qquad \text{(III.26)}$$

Differentiating Equation III 21 with time and rearranging it, we can obtain:

$$\frac{dC_L}{dt} = (C_{Max} - C_O)\frac{M}{1}\frac{t^{M-1}}{t_f^M}. \quad \text{or} \quad \frac{t}{M}\frac{dC_L}{dt} = (C_{Max} - C_O)\left(\frac{t}{t_f}\right)^M \qquad \text{(III.27)}$$

After rearranging **Equation III.6**, the last term of **Equation III.24** becomes:

$$\frac{n}{M}\frac{dC_L}{dt} \qquad \text{(III.28)}$$

Therefore, the basic partial differential equation of Gulliver-Scheil model for the dendrite arm coarsening becomes:

$$C_L(1-k)\frac{df_S}{dt} = (1 - f_s)\frac{dC_L}{dt} + b\frac{dC_L}{dt} \qquad \text{(III.29)}$$

Integrating **Equation III.29** from 0 to f_s for f and from C_O to C_L for C_L, we can obtain:

$$C_S = kC_o\left(1-\frac{f_S}{1+b}\right)^{k-1} \qquad \text{(III.30)}$$

Similarly, it can be easily shown that the analytical solution of Eq.6 for the parabolic growth rate becomes:

$$C_S = kC_O\left(1-f_S\left(\frac{1-2k\Omega}{1+b}\right)\right)^{\left(\frac{k-1}{1-2k\Omega}\right)} \qquad \text{(III.31)}$$

M can be calculated by using a fitting program between the exact solution and this analytical model.

For constant cooling, M is computed as a function of n and k by comparing the exact numerical Model of Kirkwood with **Equation III.30** whereas, for parabolic solid growth, M is obtained by comparing the Vollerôs parabolic solid growth model with the **Equation III.30**[8]

$$\text{where } b=\frac{n}{M}=\frac{n}{\left(\frac{1.2+2.4n^{0,7}}{k}\right)} \qquad \text{for constant cooling} \qquad \text{(III.32)}$$

$$b=\frac{n}{M}=\frac{n}{\left(\frac{41.12+51.59n^{0,12}}{k}\right)} \quad \text{for solidification controlled by parabolic solid growth.} \qquad \text{(III.33)}$$

MODEL IN MICROSEGREGATION

Kattamis and Flemings gave a model for microsegregation and its homogenization by heat treatment. An elementary way of looking at this is to consider the distribution of solid across a dendrite, using the Sheil analysis **Figure III.15.(a)**. This gives the plotted solute concentrations at 1, 2, 3, and 4. In a rough approximation, across a solidified casting, the solute may be taken to vary sinusoidally **Figure III.15.(b)**. [17]

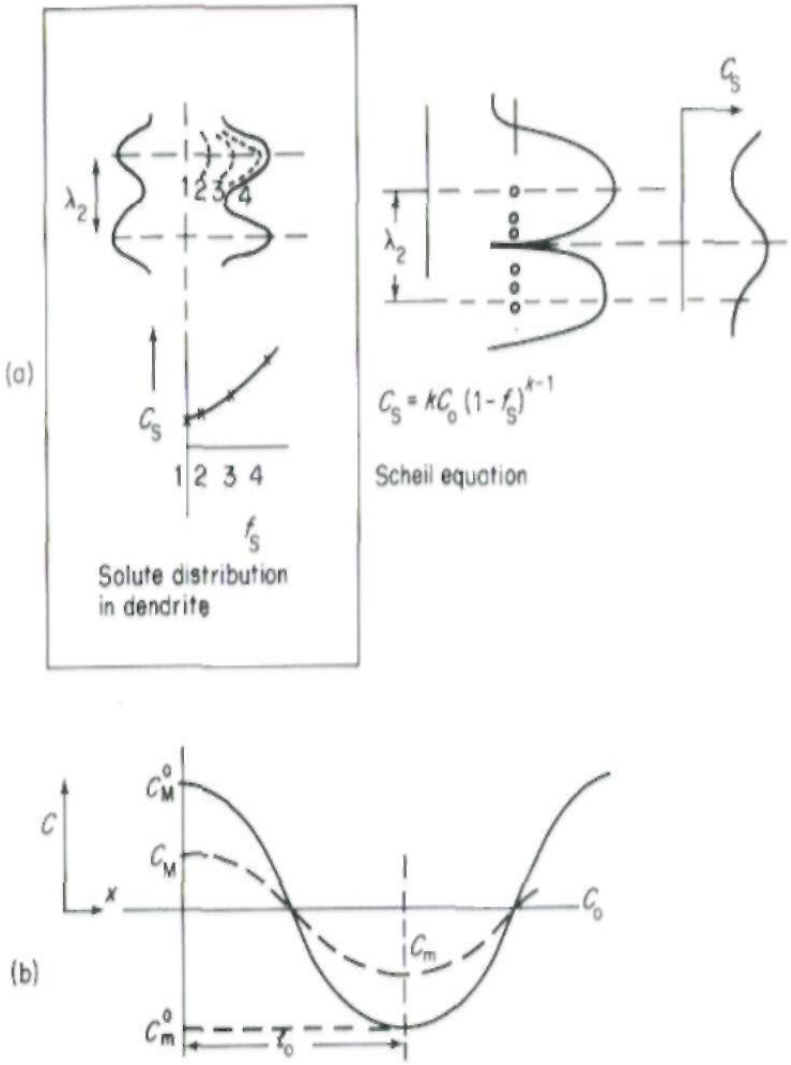

Figure III.15.(a) Solute distribution in dendrite calculated from Scheil equation, (**b**) Variation of solute distribution in dendritic structure on annealing. C^0 is minimum solute content (at centre), C_m^0 is maximum solute content (at exterior), C_m and C_M are new minimum and maximum at end of annealing period. After Kattamis and Flemings [17]

content (at the centre of a dendrite) and C_M^0 is the maximum solute content (toward the dendrite exterior), the distribution will vary with thermal treatment. After a time t at a temperature where D_s is the diffusion coefficient of solute, the new distribution will be C_m and C_M. An index of residual segregation was defined as follows: [17]

$$\delta_i = \frac{C_M - C_m}{C_M^0 - C_m^0} \qquad \text{(III.34)}$$

This can be approximately related to the diffusion of solute by: [1]

$$\delta_i = \exp\left(-\frac{\pi^2 D_s t}{L^2}\right) \qquad \text{(III.35)}$$

where $L = \lambda/2$ = one-half the dendrite spacing, and thus the time can be evaluated for any treatment reducing the residual segregation to δ_i. [17]

PART IV

EXPERIMENTAL PROCEDURE

IV.1.EXPERIMENTAL PROCEDURE

Microsegregation occurs in dendritic and cellular microstructures as a result of non-equilibrium solidification and can affect physical and chemical properties of cast structures, such as corrosion, mechanical properties and phase transformations, banding structure, amount of eutectic phase, solution and homogenization heat treatments. In this study we chose 4140 low alloy steel because of its large applications in machine constructions. In this thesis, we focused and investigated mainly microsegregation of Mn, Mo and Cr elements in directionally solidified 4140 alloy and their distributions in dendritic structure. Typical composition of 4140 is given in **Table IV.1**

Table IV.1 Typical composition of 4140 steel

4140 Steel	C	Mn	Si	Cr	Mo	S	P
	0,40	0,70	0,25	1,00	0,20	0,040	0,040

IV.1.1.Directionally Solidification and Casting

We designed a special equipment to obtain directionally solidified 4140 low steel alloy **Figure IV.1**. In the ideal directional solidification, heat extraction should occur only from one direction. In other axes heat flow should be minimized with good insulation. In order to do this, we used water cooled brass chill at the bottom to initiate solidification whereas special mould materials were used in order to minimize heat loss from the surface of the cylindrical mould. After pouring molten alloy into mould, water cooling system is opened to cool brass chill during casting.

At the beginning we heated the cylindrical mould up to 1100 ^{O}C in a furnace and also heated brass chill surface to minimize heat loss when mould is contacted with brass chill. 4140

n furnace **Figure IV.2**. In order to obtain the possibility ter casting, alloy especially overheated up to 1600 C^0. After deoxidation with Al, molten alloy was poured into heated mould. Top of mould was covered with insulation materials to minimize heat loss from the surface, i.e. radiation from surface.

Typical directional solidification equipment and its mould design can be seen in the **Figure IV.1**. As it can be seen in these photographs the water cooled brass is at the bottom and mould is located on it.

Figure IV.1 Directional solidification equipment

Figure IV.2 Melting alloy in an induction furnace

IV.1.2.Macroscopic and Microscopic Examination

Having removed the cast specimen from the mould it was cut longitudinally into two pieces to investigate columnar macrostructure. After coarse polishing, 40 % HCl+20 % HNO_3 + hot water solution (70^{o}C) was used as macro-etcher for 45 minutes to identify dendritic columnar structures. Following this macroscopic examination, specimen cut to 30 mm long samples because the bakelite mounting press can allow a maximum length of sample equal to 30 mm. Each piece was mounted in bakelite. Then the specimens were coarse-polished and fine diamond polished up to 0.25 micron. After color etching with 4 % picral + alcohol and $K_2S_2O_5$ (5gr), fine dendritic structures were clearly revealed. [18,19]

IV.1.3.Secondary Arm Spacing Measurements

A simple method was used for measurement of secondary dendrite arm spacing. After taking the sequential photographs of the longitudinal sections, and printing them or projected onto a wall, secondary arm spacing can be measured on the photographs or on the wall. We

Before taking micro-photographs of samples, a special graphs were taken at each magnification. The length of calibration bar is 1 mm at 1 magnification so that we can easily calculate the average dendrite arm spacing in each region **Figure IV.3**. We also measured average distance from the bottom using same calibration. Therefore measured secondary arm spacing can be easily plotted as a function of distance from chill. If there was any error in the measurements, it arose from the sectioning of the specimen. But also this was overcome by measuring several (at least five or six) dendrite arms in the same region.

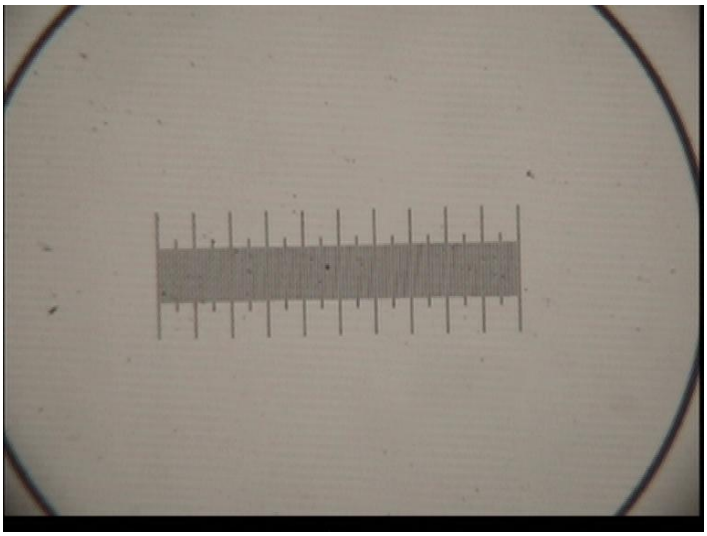

Figure IV.3 The photograph of calibration bar (X50)

IV.1.4.Microsegreagtion Measurements

Following metallographic examination of the specimen, three different regions were selected in order to analyze the segregation of Cr, Mn, and Mo elements in directionally solidified dendritic structure of 4140 steel. Several secondary dendrite arms were line-analyzed at three different distances from cold chill on the longitudinal sections, so that the change in segregation ratio (Cmax/Cmin) of each element was obtained. Usually four to ten secondary arms were line-analyzed and the average was taken to represent the region.

e also line-analyzed segregation of Mn, Cr, and Mo direction (to primary arms). From this kind of analyzes we can obtain some data for the segregation of these elements between primary arms

Microprobe (MP) and scanning electron microscope (SEM) was used in this thesis for segregation measurement. Because pure iron and manganese samples in the microprobe were oxidized, we couldouly analyze than one specimen. This measurement did not give good results. After presenting this thesis, some more analysis will be carried out with microprobe to increase number of measurements and also we hopefully do some concentration map with this, so that segregation of these elements in dendritic structure will be revealed and compared microsegregation models.

PART V

V.1.RESULTS

V.1.1.Dendritic Structure

Typical directionally solidified specimen and their dendritic structure are shown in the **Figure V.1**. As it can be seen in this figure, 4140 alloy, at the bottom or near the chill region, solidifies so quickly that very fine structure zone occurs. Secondary arm spacing increases almost linearly with distance from the bottom to the end of columnar zone under our experimental conditions. It means that cooling rate decreases almost linearly in this region. Another interesting point is that structure totally consists of columnar dendrites. This means that there is a good directional heat flow maintained at the bottom of the specimen. However, this zone was not very large. This zone length was almost 6 cm under our experimental condition. In order to increase the columnar zone, we should improve the directional solidification equipment and radial insulation.

We can also clearly recognize from the **Figure V.1** that segregation of Cr, Mn, and Mo are mainly between primary arms rather than secondary arms. Color difference indicates this in the microstructure. At the high magnification, this can be seen more clearly as shown in **Figure V.2, 3 and 4.** Another interesting point is that some spot segregation can be easily recognized. These regions are mainly last solidification regions in the single phase solidified alloys (or with very little eutectic structure) between primary arms surrounded by secondary arms. In these spot segregation regions, concentration of solute elements can rise much higher than other region, therefore inclusion or porosity can form there.

acing Measurement

As described in the experimental procedure, secondary arm spacing was measured on the longitudinal section as a function of distance from the bottom of specimen in the figure 1. These data were plotted as shown in the **Figure V.5.** It is clear from this figure that although there is large variation of secondary arms in each region, secondary arm spacing increases with distance almost linearly from 30 micron to 85 micron from the bottom of specimen to the end of columnar zone. Using regression method this curve can be expressed as given below.

$$\lambda_2(\mu m) = 29.522 + 1.3593 * dis\tan ce(mm) \qquad r^2=0.6852$$

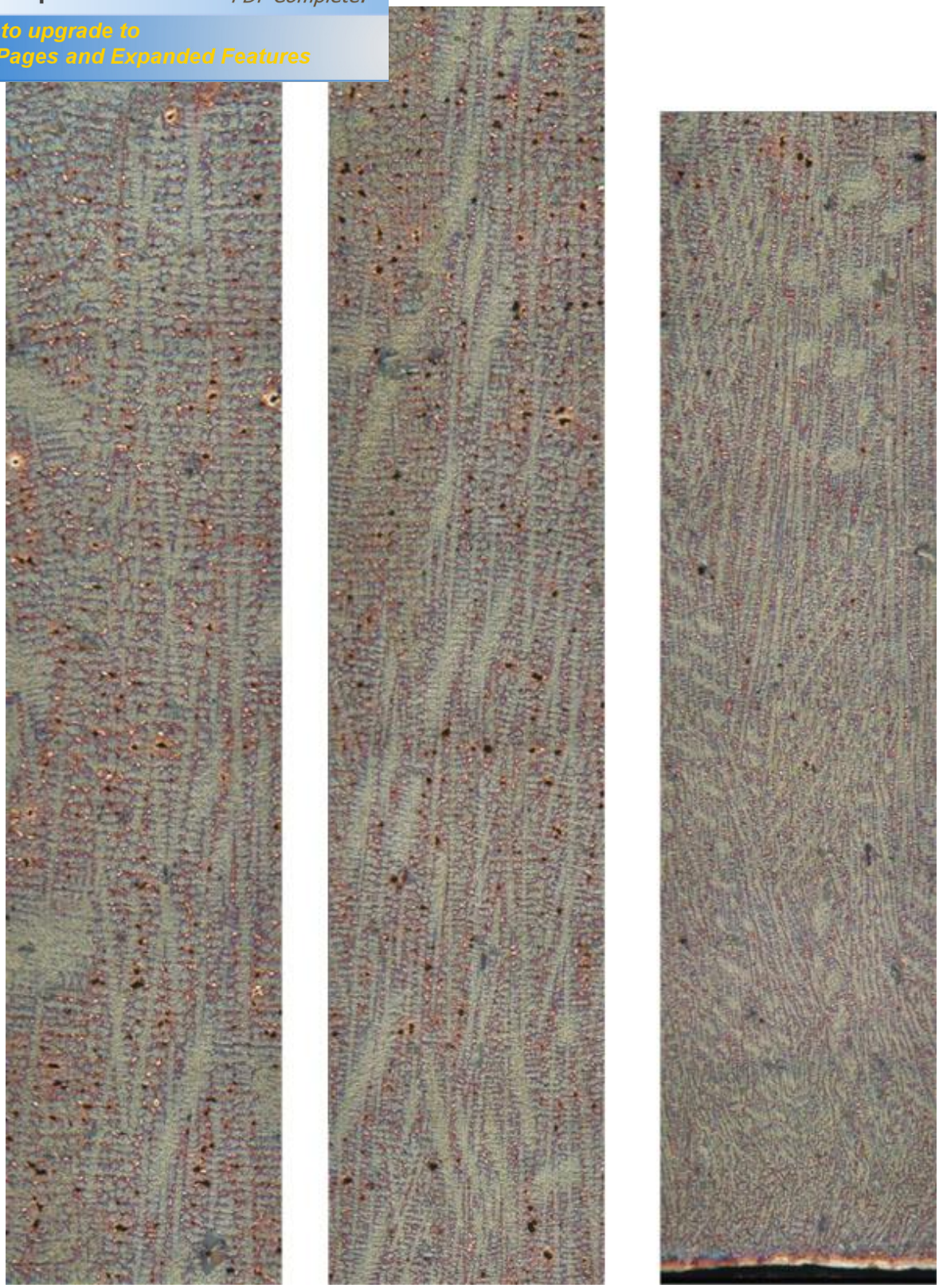

Figure V.1 Photograph of the longitudinal section of 4140 steel showing the highly segregated lines between primary arms and the change of the secondary arm spacing as a function of distance from chill. (X50)

Figure V.2 Highly segregation lines between primary arms (X50)

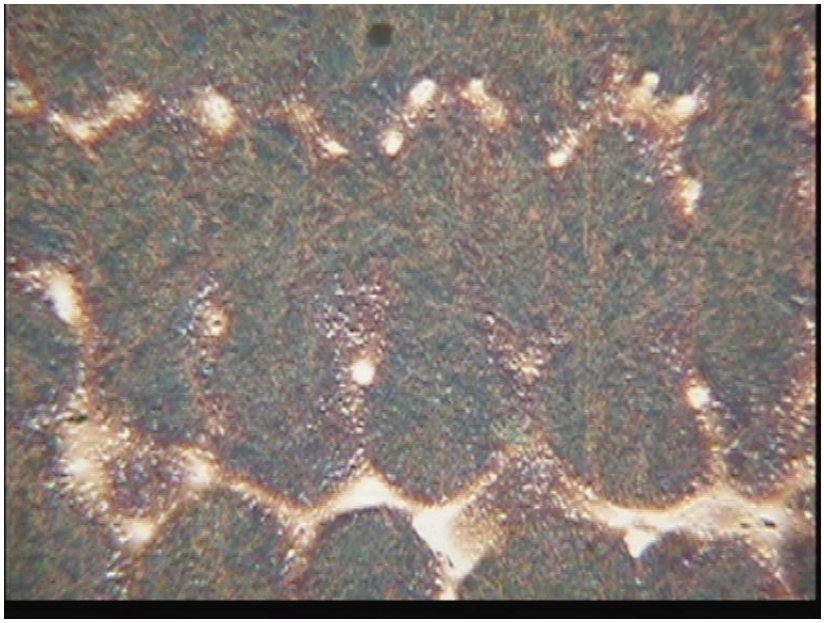

FigureV.3 Highly segregation lines between primary arms and some spot segregation points between primary arms surrounded by secondary arms (X200)

Figure V.4 Some spot segregation point at the high magnification (X500)

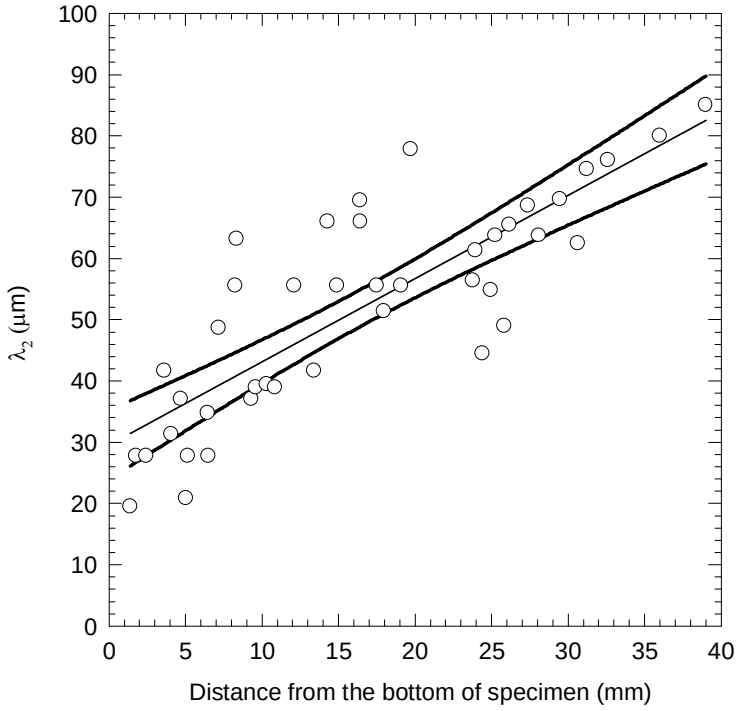

Figure V. 5 Change of secondary arm spacing as a function of distance from chill

ırements

We investigated microsegregation of main alloying elements (Cr, Mo, and Mn) in 4140 steel. Two analysis were done in three different region. One of them is parallel to the primary arm spacing and the other one is perpendicular to primary arms spacing, therefore segregation can be related to distance as well as to dendritic morphology. From first analysis we obtained some values for segregation of Cr, Mo, and Mn elements between secondary arms and from the second one for segregation data between primary arms. Obtained concentration profiles and their microstructures are given in **Figures V.6, 7, 8, and 9** for each region. It may be noticed in concentration profiles that we can not obtain concentration in each region with this method. However, concentration difference can be seen as count per second (cps) on y axis, therefore we easily calculate average microsegregation ratio as S=Cmax./Cmin in each region. Average calculated segregation ratios are given in **Table V.1**.

Table V.1 Average segregation ratio in 4140 steel.

S=Cmax./Cmin Near to chill (parallel to primary arms.)
Cr=1,5
Mn=1,66
Mo=1.7
S=Cmax./Cmin Near to chill (per particular to primary arms.)
Cr=1,75
Mn=1.8
Mo=1.9
S=Cmax./Cmin Near to the end of columnar zone.(parallel to primary arms.)
Cr=1,8
Mn=2
Mo=1,2
S=Cmax./Cmin Near to the end of columnar zone.(per particular to primary arms.)
Cr=1,75
Mn=2
Mo=2

en
Mn=2
Mo=1,7

As can be seen from this table microsegregation ratios of all alloying elements are mainly between 1.5 and 2. Segregation ratios of Cr, Mn and Mo elements between secondary arms are less than between primary arms. This is consistent with the color micro-photographs. It is also noticed that segregation ratios of alloying elements decrease slightly with distance, approximately from 2 to 1.5.

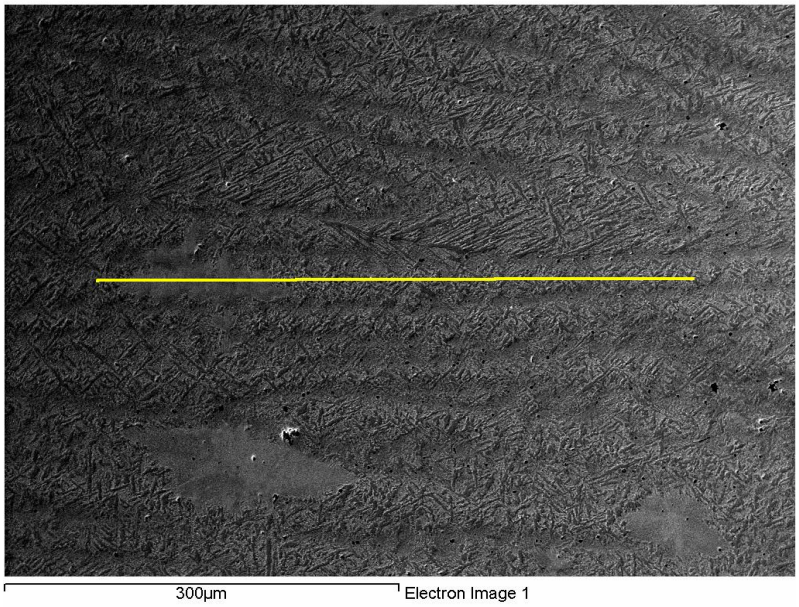

Figure V.6 a. Micrograph near to chill showing the analyzed line parallel to primary arms

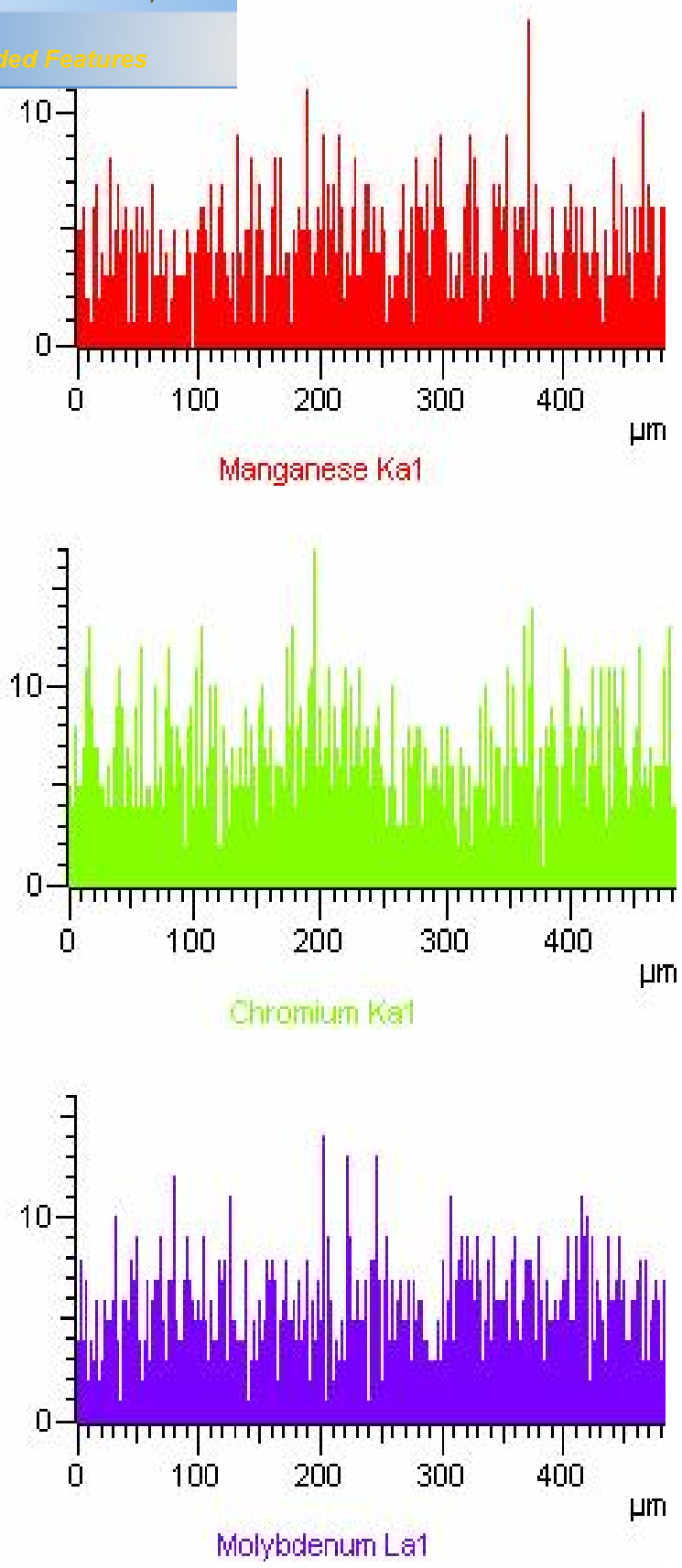

Figure V.6.b Concentration profile for each element through the line (near to chill)

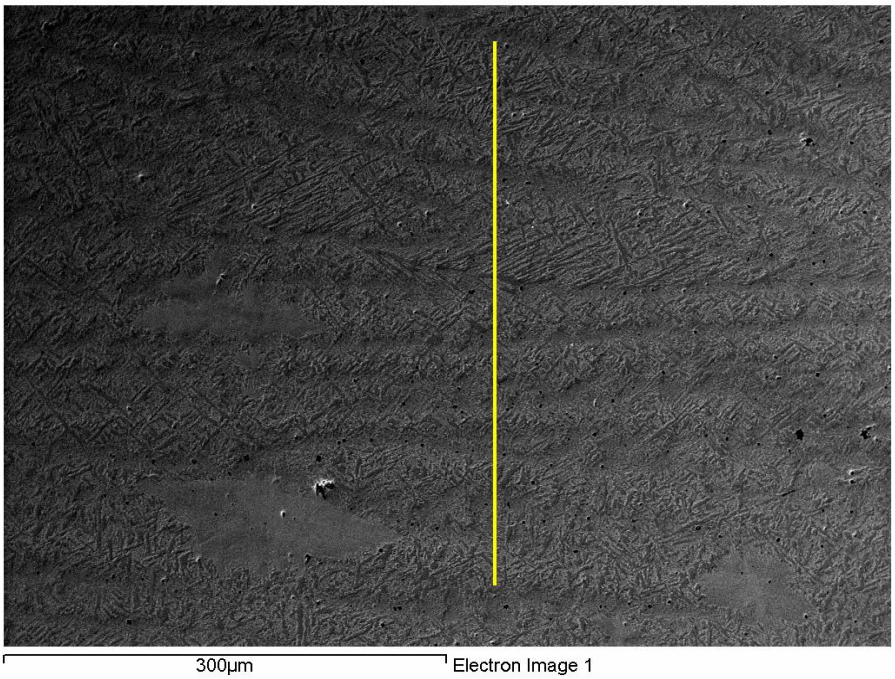

Figure V.7 a Micrograph near to chill showing the analyzed line perpendicular to primary arms

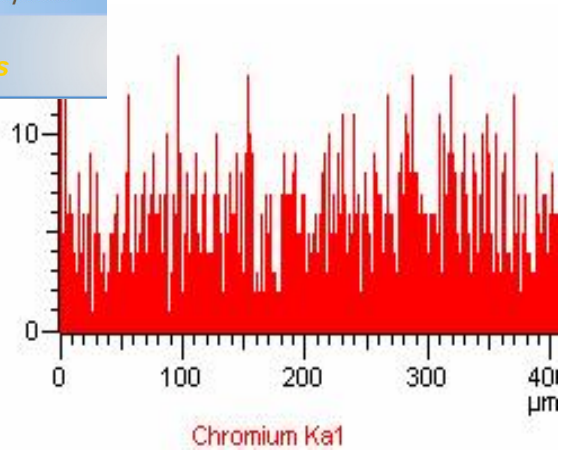

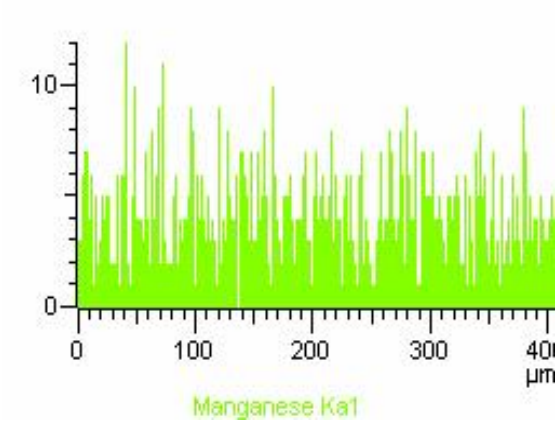

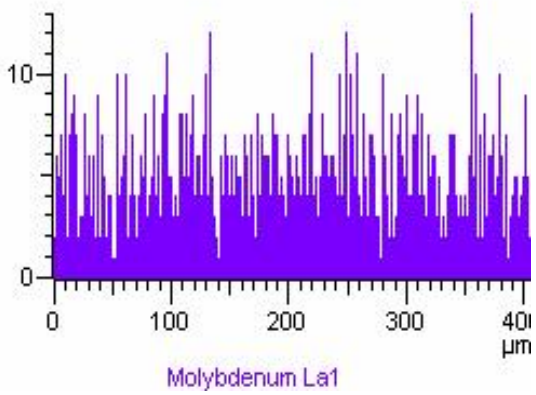

Figure V.7 b Concentration profile for each element through the line (near to chill)

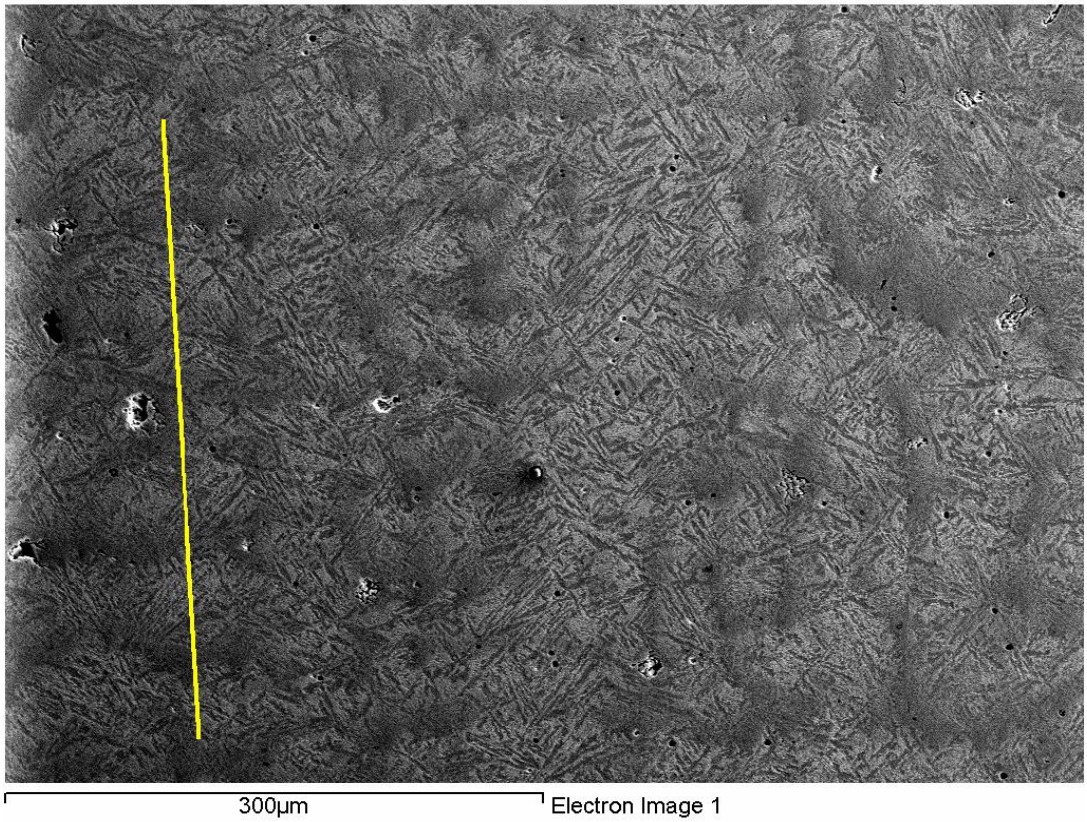

Figure V.8 a. Micrograph near to the end of columnar zone showing the analyzed line parallel to primary arms

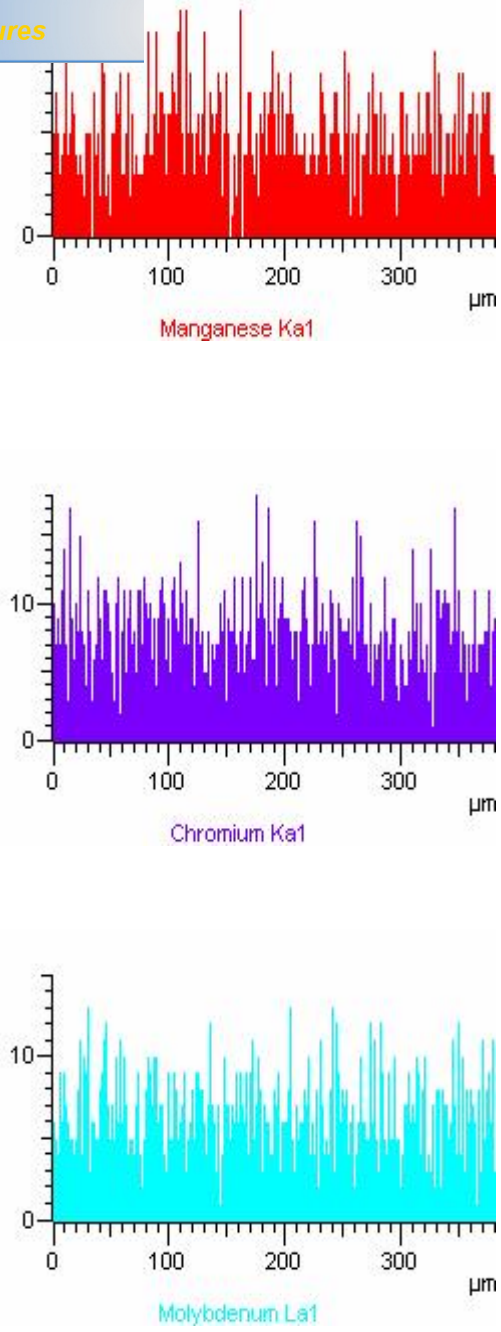

Figure V.8 b. Concentration profile for each element through the line (near to the end of columnar zone)

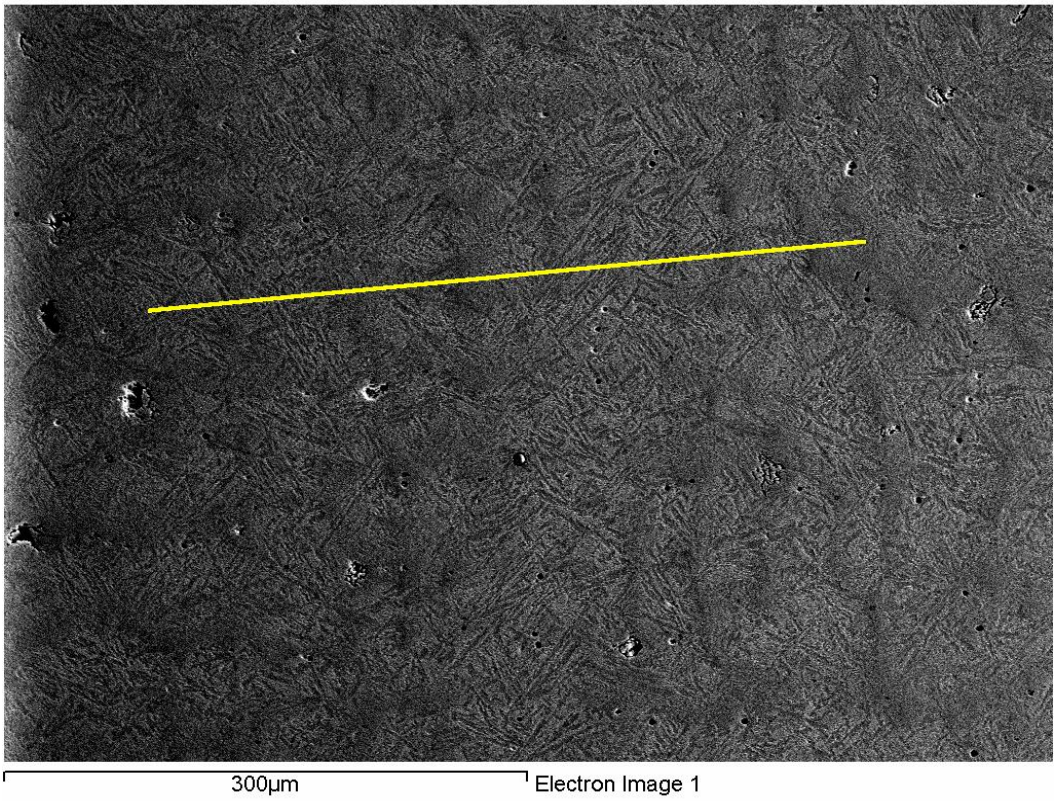

Figure V.9.a Micrograph near to the end of columnar zone showing the analyzed line perpendicular to primary arms

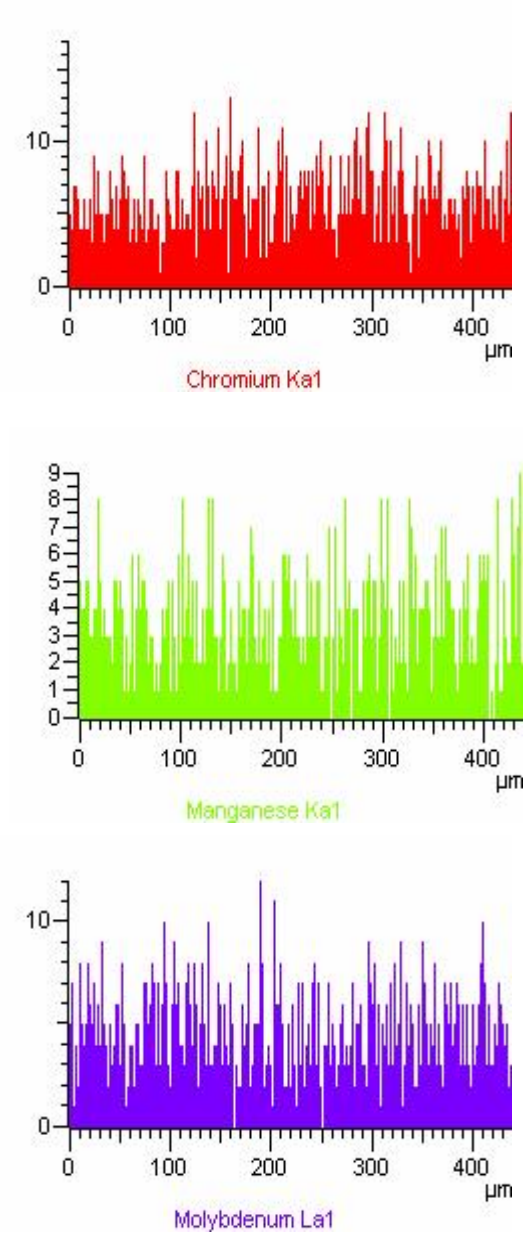

Figure V.9.b Concentration profile for each element through the line (near to the end of columnar zone)

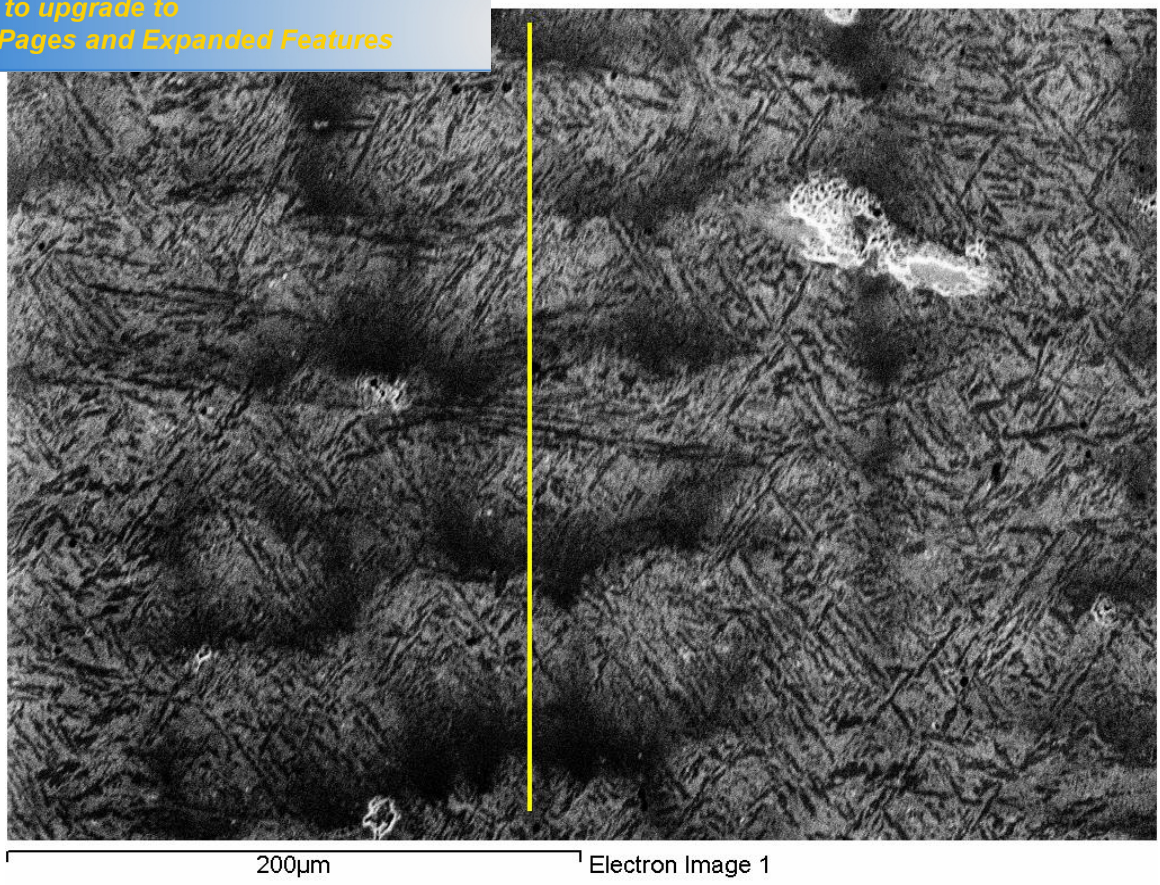

Figure V.10.a Micrograph from the middle of specimen showing the analyzed line parallel to primary arms

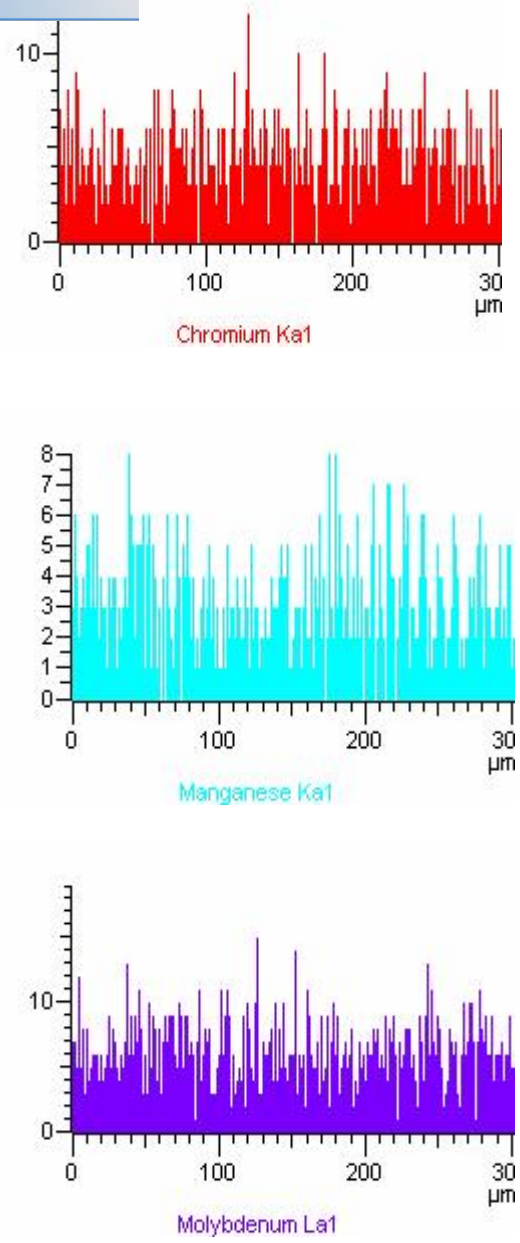

Figure V.10.b Concentration profile for each element through the line (from the middle of specimen)

DISCUSSION

VI.1.DISCUSSION

It is well known that secondary arm spacing is directly related to solidification time. If solidification time of an alloy increases by decreasing cooling rate, secondary arm spacing also increase because it contact with liquid for longer time, i.e. there is more time available for coarsening of secondary arms [17,11,4]

We compared our results with data available in literature. Polish and Flemings investigated dendritic structures as a function of distance in directionally solidified 4340 steel as shown in the **Figure VI.1** [23]. Although their composition is slightly different, i.e. it contains approximately 1.7 wt % Ni in addition to the composition of 4140 steel, our secondary arm spacing measurements give almost same result as their measurements. By comparing both figures[**Figure V.5**. and **Figure VI.1**], it may be also noticed that their columnar zone length is almost 3 times larger than our zone length. This can be attributed to our poor insulation in our casting. We can also concluded from this comparison that nickel does not affect secondary arm spacing very much, in these kind of steel because its effect on solidification range and surface energy is not very much. This conclusion also indicates that in both castings cooling rate is almost same, at least near to chill region.

Turkeli investigated microsegregation in ternary Fe-1.6 wt % Mn ï 0.1 to 0.8 wt C steel by quenching unidirectionally solidified specimens. He found that segregation ratio of Cmax to Cmin changes from region to region. Due to his experimental results, microsegregation between primary arms is less than between secondary arms. Last solidification region gives the highest segregation ratio. He presented these results in a figure as shown in the **Figure VI.2**. [24] It is interesting to note that we observed same kind of segregation behavior in our casting microstructures **Figures V.2, 3, and 4** although we cast our alloy under directional

n is simulated the real casting condition of columnar emperature gradient can change from region to region whereas in the unidirectional solidification the temperature gradient and growth rate are constant during solidification.

Fredriksson and co-workers investigated microsegregation in low alloy steel [20]. They found that microsegregation of Cr, Mo, and Mn elements in low alloy steels changes as a function of carbon content. Increasing the carbon content increases microsegregation ratio in low alloy steels. This can be attributed the delta-phase formation because in the delta phase diffusion of solute elements is almost 30-40 times higher than gamma phase. We compared our results with their measurement as shown in **Figures VI.3, 4, and 5**. As can be seen from these figures our average microsegregation ratios are slightly higher than their results.

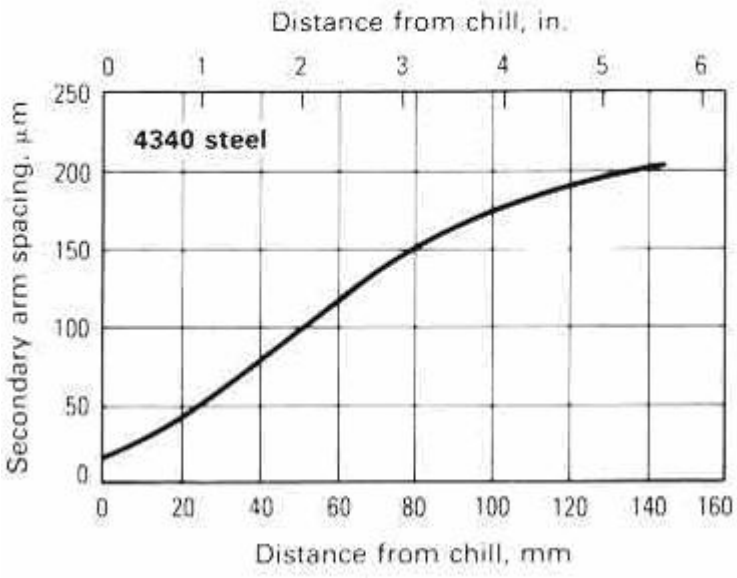

Figure VI.1 Spacing between adjacent secondary arms in dendrites of directionally solidified 4340 steel castings as a function of the distance of the secondary arms from the surface that was against a chill [21]

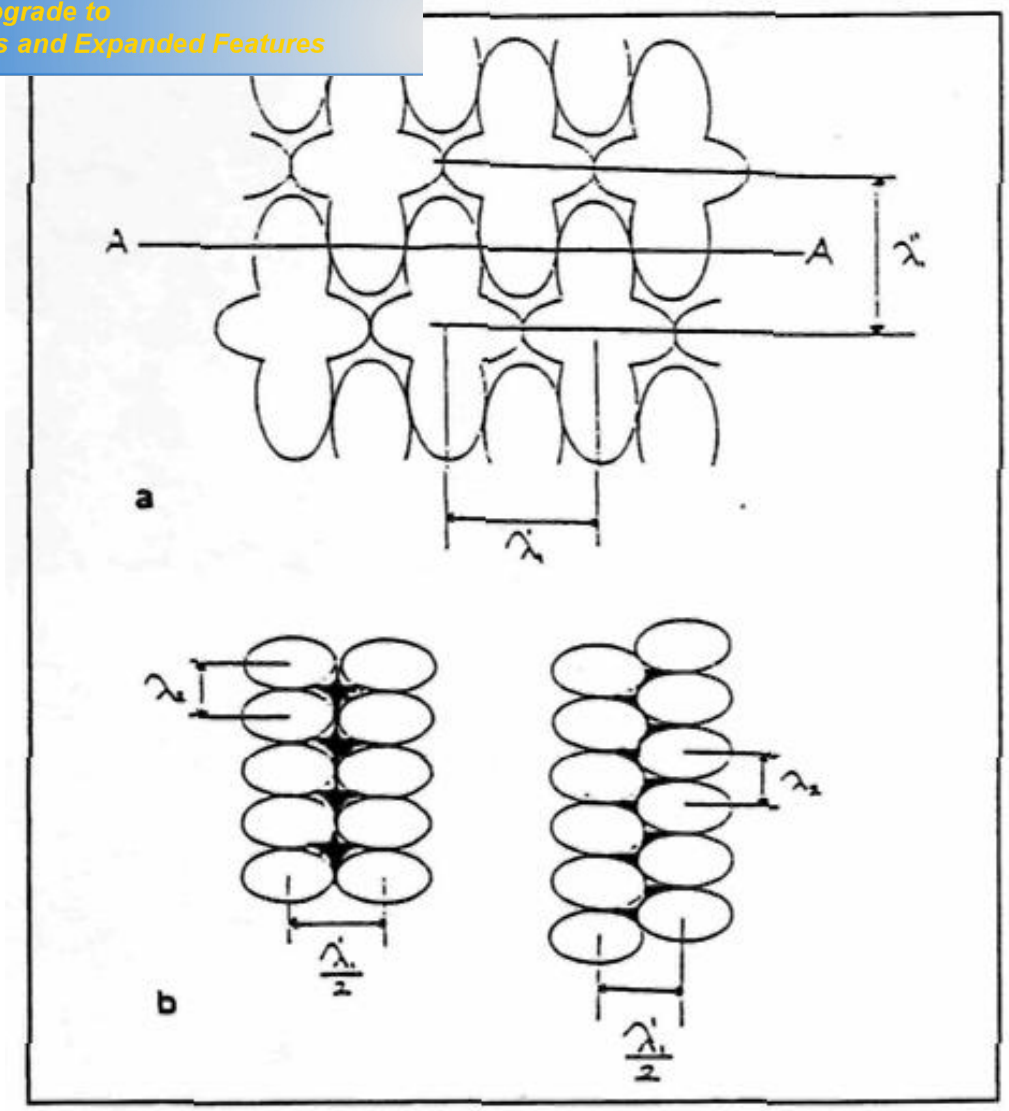

Figure VI.2 a) The transverse section of close packed primary arm spacing arrangement b)The two extreme possible arrangement of secondary arms on the longitudinal section showing concave solidification model [22]

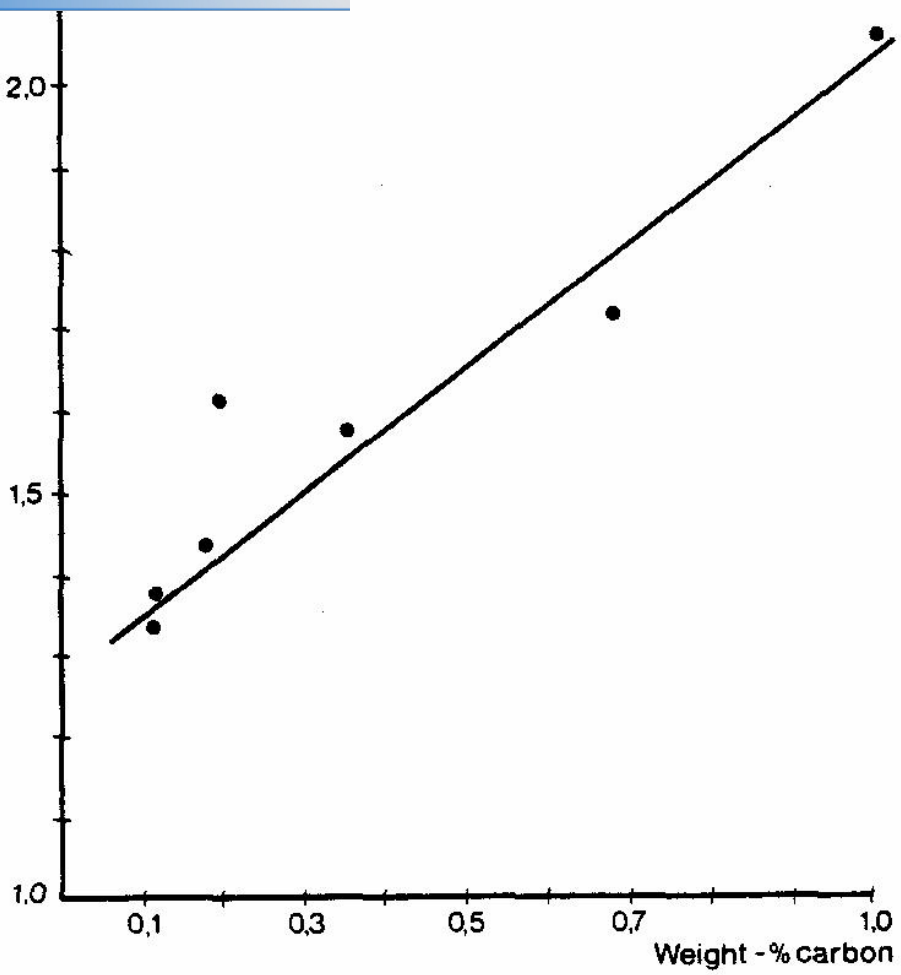

Figure VI.3 Microsegregation of manganese in carbon steels [20]

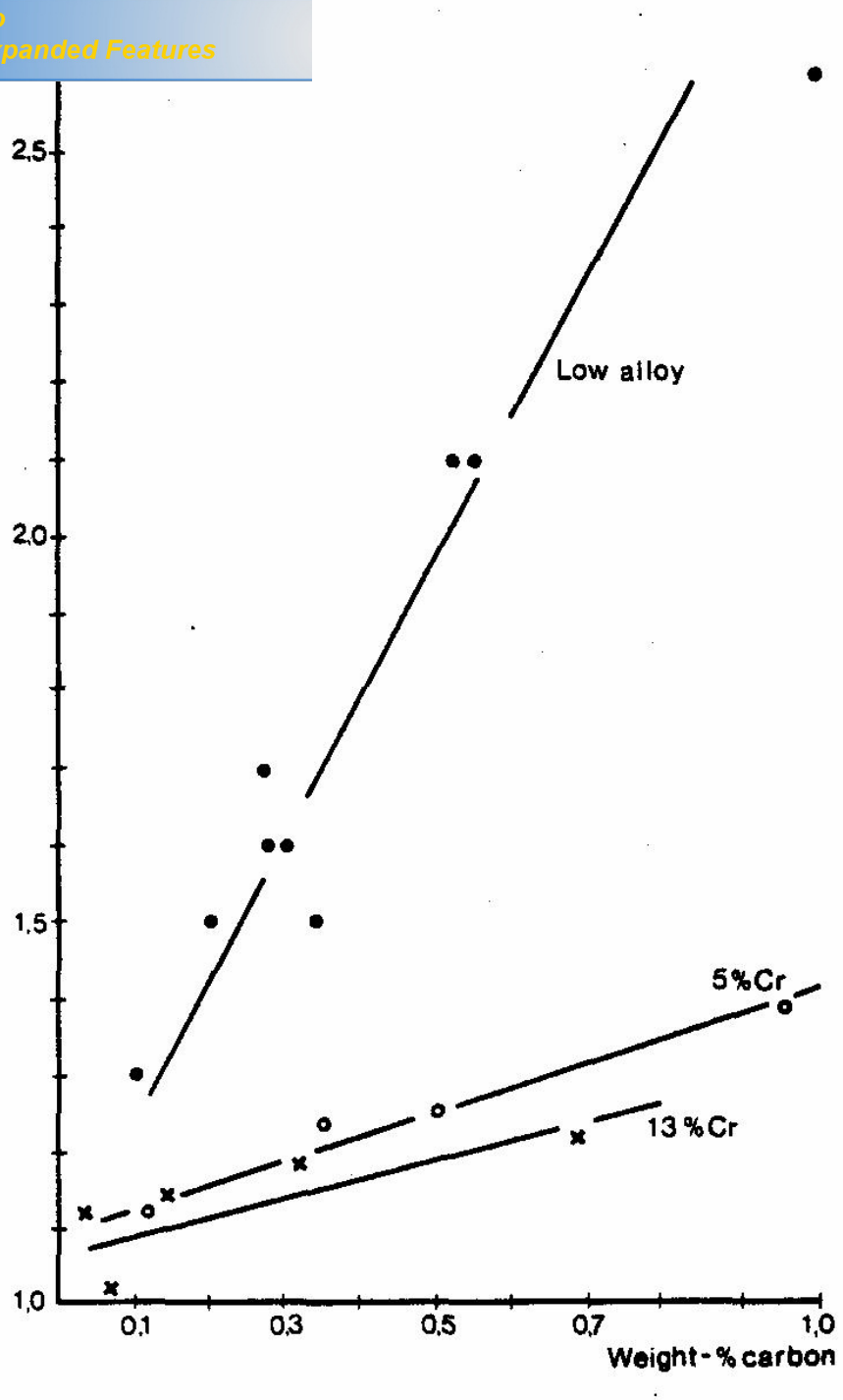

Figure VI.4 Microsegregation of chromium in low alloy steel and chromium steels [20]

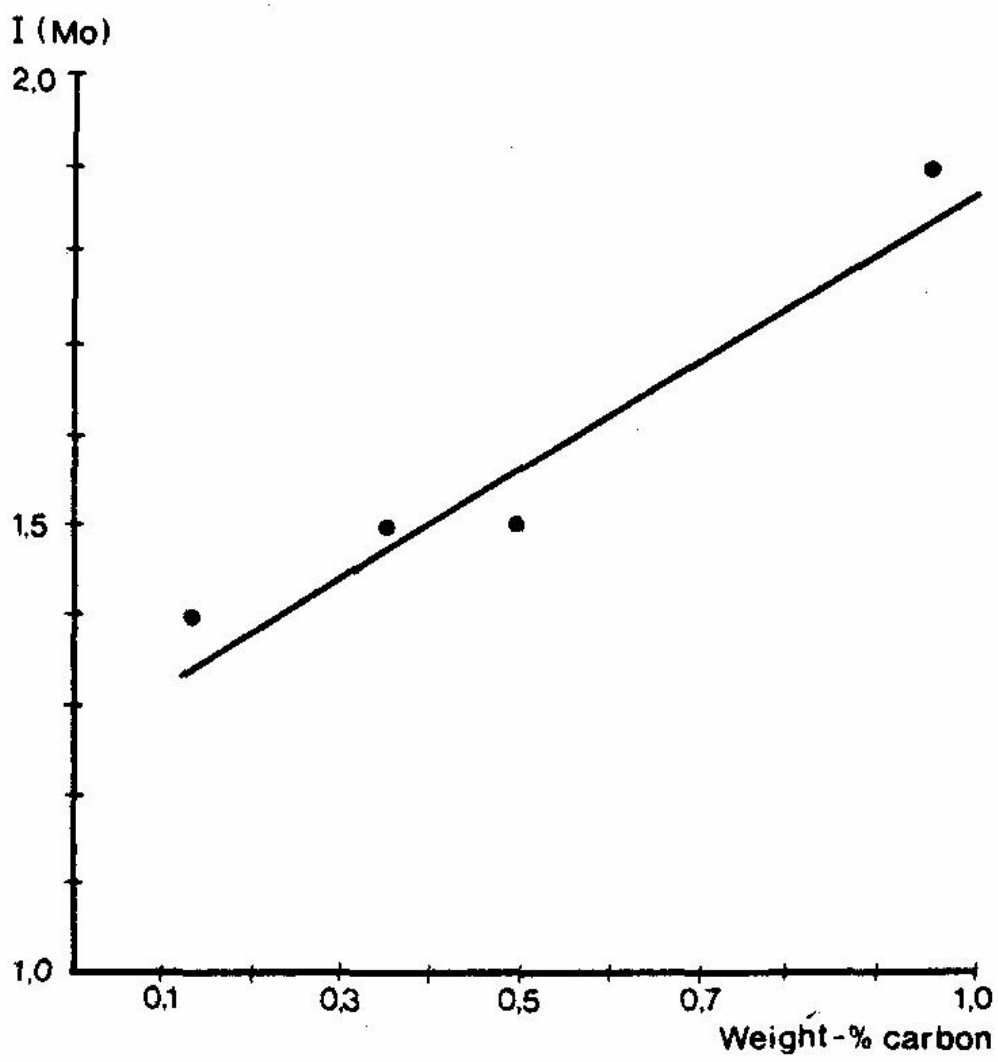

Figure VI.5 Microsegregation of molybdenum in carbon steels [20]

PART VII

CONCLUSION

VII.1.CONCLUSION

In this thesis we investigated microsegregation of solute elements (Cr, Mn, Mo) and dendritic structure in directionally solidified 4140 steel. It is found that microsegregation ratios of solute elements between secondary arms are less than that between primary arms. Microsegregation ratios in last solidification points between primary arms surrounded by secondary give the highest value. This result is in good agreement with literature.

We measured also secondary dendrite arms as a function of distance from chill. It is found that secondary dendrite arm spacing increases from 30 micron at the chill zone to 80 micron at the end of columnar zone. Comparisons between our results and data available in the literature indicate that there is a very good agreement between them.

REFERENCES

[1] http://www.matter.org.uk/matscicdrom/manual/nu.html Nucleation in Metals and Alloys Andrew Green. MATTER Phill Prangnell, *UMIST/ Manchester Materials Science Centre UK,(*June, **2007**)

[2] Chalmers, B. ***ñPrinciples of Solidificationñ*** John Wiley and Sons Ltd., New York, USA, **(1964)**

[3] Robert W. CATH and Peter HAASEN, ñ*Physical Metallurgy*ò, 2nd Ed., Volume 1, Elsevier Science B. V., Netherlands, **(1996)** 164-175

[4] C. Flemings MERTON, ñ*Solidification Processing*ò, Mcgraw-Hill, New-York, USA, **(1974)** 134-146.

[5] Warren J.A. and W.J. Boettinger,***òActa Metalò*** , **(1995)** 43

[6] Cohen M. and M.C. Flemings ***ñRapidly Solidified Crystalline Alloysò*** Warrendale, USA, **(1985)** 3

[7] Kurz W. And D. J. Fisher ,***òFundamentals of Solidificationò***, Trans Tech Publication, Switzerland, **(1998)**

[8] Burden, N.H. and J. Hunt, J. Crystal Growth, **(1974)**, 22

[9] Bouchard, D. and J.S. Kirkaldy, Metall. and Mater. Trans, 28B, **(1997)** 651

[10] Turkeli Altan, Modelling of Casting, Welding, and Advanced Solidification Processes-XI, Ed. By C.A. Candin and M. Bellet, a publication of TMS, USA, Opie, France,**(2006)** 585-592

[11] Doru Michael STEFANESCU, ñ*Science and Engineering of Casting Solidification*ò, Kluwer Academic/Plenum Publishers, New-York, USA., **(1984)**.

[12] Trivedi R. And W. Kurz ***ñMetals Handbook Ninth Editionò*** Vol.15 , ASM International, Ohio, USA, **(1988)** 114

[13] Flemings M.C., T.Z. Kattamis and B.P. Bardes.,***òMetall Trans.ò*** AFS Trans, New York, USA **(1991)** 501

[14] Kattamis T.Z. and M.C. Flemings , ***ñTrans. Met. Soc.ò***, AIME **(1965)** 992

[15] Doru Michael STEFANESCU (Volume Chair), *ASM Handbook Casting*, ASM International, 9th Ed., Volume 15, USA, **(1998)**

[16] Turkeli, A., Materials Science Forum, Vols. 508, **(2006)** 449-454

*d Cast Structure*ò, John Wiley and Sons Ltd., UK,

[18] *ASM Handbook*, Desk Edition, Ohio, USA, **(1985)** 35

[19] *ASM Handbook*, Vol.9, Ohio, USA, **(1993)** 333-340

[20] *A Guide to Solidification of Steels*, Fredriksson, , Stockholm, Sweden, **(1977)**

[21] R.F. Polish and M.C. Flemings, ñ*Mechanical Properties of Unidirectional Steel Castings*ò Trans. Am. Foundrymenôs Soc. Vol. 73, **(1965)** 28-33

[22] Turkeli, Altan and Kirkwood, David, H., ,4th International Conf. On Soliidification Processing, Ed. By H. Jones and H. Beech, Sheffield, UK, **(1997)** 308-311

MARMARA UNIVERSITY

THE INSTITUTE FOR

GRADUATE STUDIES IN PURE AND APPLIED SCIENCES

ACCEPTANCE AND APPROVAL DOCUMENT

THE DIRECTIONAL SOLIDIFICATION AND MICROSEGREGATION IN LOW ALLOY

Established committee listed below, on 17/07/2007 and 2007/11-13 by the *INSTITUTE FOR GRADUATE STUDIES IN PURE AND APPLIED SCIENCES*' Executive Committee, have accepted Mr. Özgür Çınar's Master of Science / Doctor of Philosophy thesis, titled as "The Directional Solidification and Microsegregation In Low Alloy Steel in Metallurgical and Material Engineering.

COMMITTEE

Advisor : Prof. Dr. Altan Türkeli .....

Member : Yrd. Doç. Dr. Kenan Yıldız.....

Member : Yrd. Doç. Dr. Seval Genç.....

Date of thesis' / dissertation's defense before the committee:17/07/2007

APPROVAL

Mr. Özgür Çınar has satisfactorily completed the requirements for the degree of Doctor of Philosophy / Master of Science in Material Science and engineering..... at Marmara University.

Mr. / Mrs. / Miss. Özgür ÇINAR..... is eligible to have the degree awarded at our convocation on 12.11.2007 2007/25-15 Diploma and transcripts so noted will be available after that date.

Istanbul

DIRECTOR

T.C. MARMARA ÜNİVERSİTESİ FEN BİLİMLERİ ENSTİTÜSÜ KURULU 1973

Prof. Dr. Sevil ÜNAL
Müdür